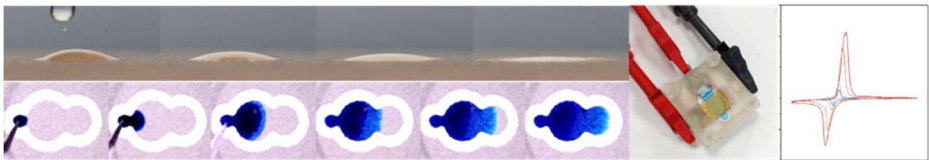**National University of Science and Technology POLITEHNICA Bucharest**

Doctoral School of Energy Engineering

Faculty of Power Engineering

Hydraulics, Fluid Machinery and Environmental Engineering Department

REOROM Laboratory

DOCTORAL DISSERTATION

Transport Processes in the Presence of Interfaces in Porous Media with Applications in Electrochemical Sensors Development

Dissertation abstract

Author: Drd. Ing. Oana Daciana Botta

Scientific coordinator: Prof. Dr. Ing. Corneliu Bălan

A thesis submitted for the degree of

Doctor of Philosophy in Engineering Sciences

BUCHAREST

2024

National University of Science and Technology POLITEHNICA Bucharest
Doctoral School of Energy Engineering
Faculty of Power Engineering
Hydraulics, Fluid Machinery and Environmental Engineering Department
REOROM Laboratory

DOCTORAL DISSERTATION

Transport Processes in the Presence of Interfaces in Porous Media with Applications in Electrochemical Sensors Development
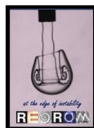**Dissertation abstract**

Author: Drd. Ing. Oana Daciana Botta
**Scientific coordinator: Prof. Dr. Ing. Corneliu Bălan**

EVALUATION COMITEE

Președinte	Prof. Dr. Ing. Radu Porumb	de la	U.N.S.T. Politehnica București
Conducător	Prof. Dr. Ing. Corneliu Bălan	de la	U.N.S.T. Politehnica București
Referent	Prof. Dr. Ing. Sanda Carmen Georgescu	de la	U.N.S.T. Politehnica București
Referent	C.S.I Dr. Ionuț Enculescu	de la	I.N.C.D. pentru Fizica Materialelor
Referent	Prof. Dr. Ing. Ilinca Năstase	de la	Universitatea Tehnică de Construcții din București
Membru supleant	C.S.I Dr. Eugen Gheorghiu	de la	International Centre of Biodynamics

BUCHAREST
2024

Abstract

Graphical abstract
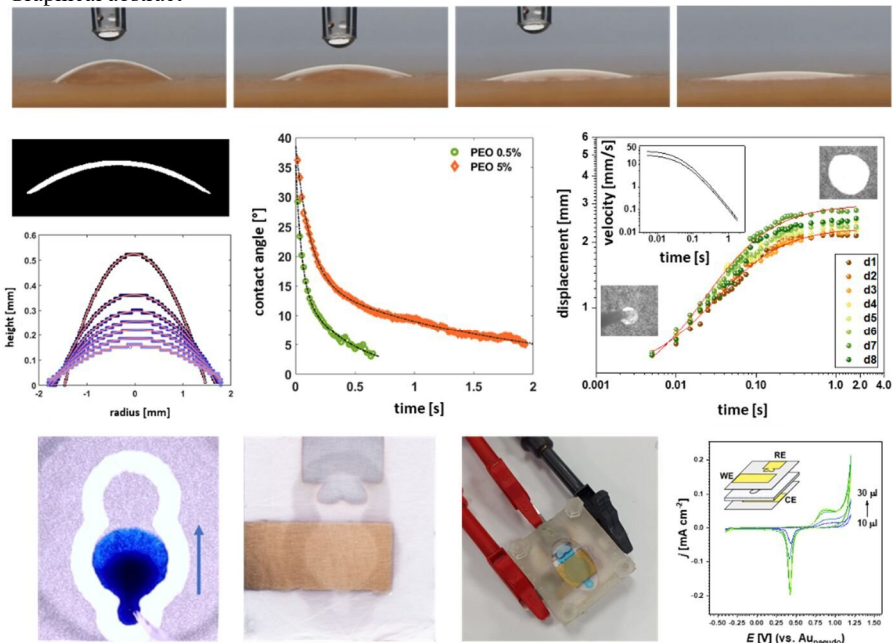
The present thesis is a contribution to the application of fluid transport phenomena in porous media for the development of electrochemical sensors. The study focuses on the experimental investigation and modelling of flow in porous media under the action of mass and capillary forces, with applications in the controlled electric charge transport in conductive porous media in the presence of a fluid. The final application of the thesis is the fabrication of a portable electrochemical cell consisting of metallised electrospun polymeric meshes deposited on a paper substrate. This is the first literature report of a sensor with such an architecture that can detect various chemical compounds in fluid media.Thus, the thesis is structured in two parts, the first one is devoted to the study of fluid wicking through porous media, represented by paper, and the second one presents the fabrication and optimization methods for fibrillar electrodes and the integrated architecture with paper.

The theoretical analysis of the phenomenon consisted in identifying the equations with which the time evolution of the wetted surface and the droplet interface can be described, and the results were evaluated using the *Mathematica* numerical code.

The experimental study was carried out for different cases of the diffusion phenomenon, and the influences of geometry of the porous medium, viscosity of fluids, and concentration of dissolved molecules in liquids were investigated. In order to streamline the analysis process, a numerical algorithm for automatic image processing was developed in MATLAB.

In the second part of the thesis, two methods for fabricating porous media with fibrillar polymer structure were experimentally investigated. The influences of material, process and environmental parameters on the morphology of the resulting fibers and surface porosity were analyzed. Subsequently, conductive layers were deposited on the surface of these materials in order to investigate electrical charge transfer at the contact interface with a fluid.

Finally, the steps required to develop an electrochemical sensor with a multi-layered porous structure, comprising an absorbent substrate for fluid retention and two layers of metallized polymer fibers acting as electrodes, are presented. The behaviour of the sensor was investigated using different conductive materials and fluids with different properties. The applicability of the sensor was investigated initially for the detection of hydrogen peroxide and subsequently for chemical compounds of biological origin. The prospects for further research include extending the applicability of the sensor for monitoring water or air quality, the assembly being a portable electrochemical cell that has been designed to allow further integration with battery-powered electronic circuits, or energy-operated installations and devices used in various applications, representing a device for fluid analysis with low-energy consumption. The steps undertaken to achieve this are shown in the flowchart below.
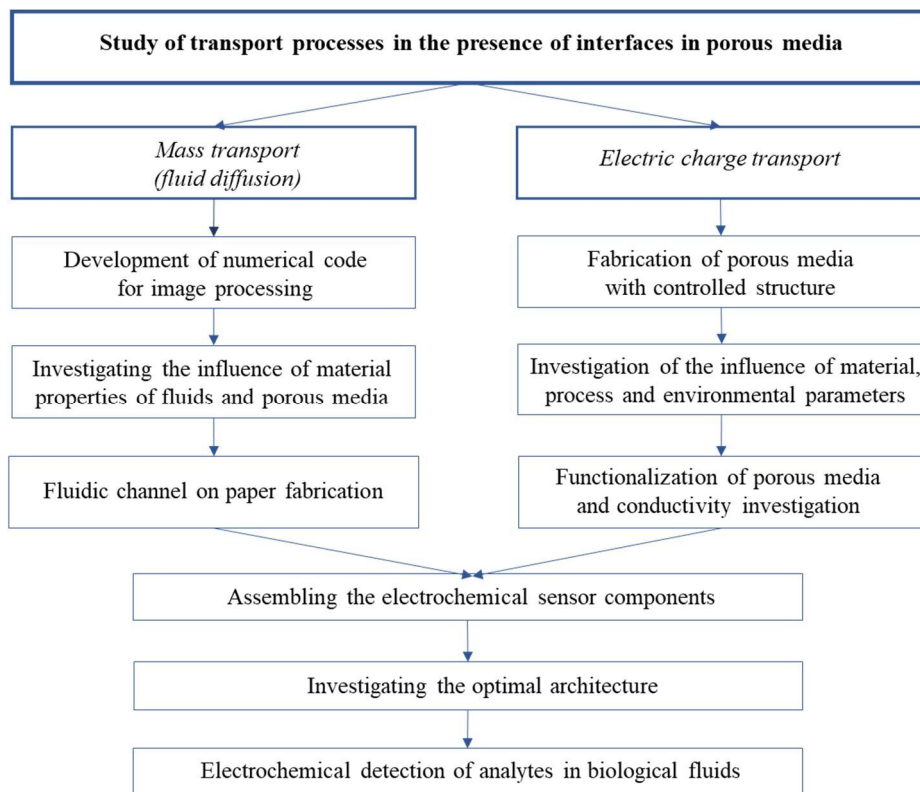
Keywords: fluid diffusion, porous media, polymer fibers, electrochemical detection.

Table of contents

List of publications

I. ISI indexed articles
1. **D. Botta**, I. Enculescu, C. Balan, V. C. Diculescu, Integrated architectures of electrodes and flexible porous substrates for point-of-care testing, *Current Opinion in Electrochemistry*, 2023, 101418, ISSN 2451-9103, 10.1016/j.coelec.2023.101418.
2. **D. Botta**, C. Bălan, Numerical Analysis of the Drop Shape During Wicking in Porous Media, *U.P.B. Sci. Bull., Ser. A.*, 85 (2023)

II. ISI proceedings and BDI
1. **D. Botta**, I. Magos and C. Balan, Influence of Viscosity on Radial Diffusion of Fluids in Paper Substrates, *12th International Symposium on Advanced Topics in Electrical Engineering (ATEE)*, 2021, 10.1109/ATEE52255.2021.9425224.
2. **D. Botta**, I. Magos and C. Balan, The Influence of Surface Tension on Radial Wicking in Paper, 2021, *10th International Conference on ENERGY and ENVIRONMENT (CIEM)*, pp. 1-5, 10.1109/CIEM52821.2021.9614767
3. **O.D. Botta**, I. Magos, C. Balan, Experimental study on the formation and break-up of fluid bubbles, *INCAS Bulletin*, 2020, 12(1), 27-34. 10.13111/2066-8201.2020.12.1.3

III. International conferences
1. **D. Botta**, A. Evanghelidis, M. Beregoi, E. Matei, I. Enculescu and V. C. Diculescu, Microfluidic Devices with Conductive Electrospun Polymeric Fibers, 74th Annual Meeting of the International Society of Electrochemistry (ISE) 2023
2. **D. Botta**, C. Sanz, M. Beregoi, E. Matei, I. Enculescu and V. C. Diculescu, Devices with Metallized Electrospun Fiber Meshes Electrodes, Biosystems in Toxicology and Pharmacology – Current challenges (BTP) 2022
3. **D. Botta** and C. Balan, Experimental Determination of Radial Wicking Velocities for Complex Fluids, Annual European Rheology Conference (AERC) 2022
4. **D. Botta**, I. Magos and C. Balan, Influence of Viscosity on Radial Diffusion of Fluids in Paper Substrates, 12th International Symposium on Advanced Topics in Electrical Engineering (ATEE) 2021
5. **D. Botta**, I. Magos and C. Balan, The Influence of Surface Tension on Radial Wicking in Paper, 10th International Conference on ENERGY and ENVIRONMENT (CIEM) 2021

IV. Member in research projects
1. Physics of Viromimetic Particles (contract no. 760099/23.05.2023 PNRR)
2. Bio-inspired semiconducting fibers for field effect transistors (PN-III-P4-PCE-2021-1131)
3. An electrochemical point-of-care device for nucleic acids quantification (PN-III-P4-PCE-2021-1006)
4. Molecularly imprinted nanofluidic biosensors for the detection of human derived proteins (ERANET-MANUNET-III-MINaFBioS)
5. Disposable nanostructured biosensors based on metallic electrospun fibers for real time monitoring of superoxide in cell cultures (PN-III-P1-1.1-TE-2019-0387)

V. Patents
- **Botta Oana-Daciana**, Diculescu Victor Constantin, Enculescu Marius Ionut, Beregoi Mihaela, Evanghelidis Alexandru, Matei Elena, Celulă electrochimică cu structură fibrilară flexibilă integrată, A 2024 00191.

- Costas Liliana-Andreea, Preda Nicoleta-Roxana, **Botta Oana-Daciana**, Ciobotaru Iulia-Corina, Enculescu Marius Ionut, Procedeu de obținere a unei diode electroluminescente pe bază de matrici de nanofire miez-coajă de tip oxid de zinc și seleniură de zinc obținute pe electrozi metalici interdigitați, A 2024 00078.
- Enache Teodor-Adrian, Costas Liliana-Andreea, **Botta Oana-Daciana**, Matei Elena, Diculescu Victor-Constantin, Metodă de fabricare a unei platforme analitice duale pentru detecție electrochimică și colorimetrică, A0075/19.11.2020

VI. Articles in writing
1. **D. Botta**, M. Beregoi, M. Enculescu, A. Evanghelidis, E. Matei, A.-M. Ignat, A. Pascu, I. Enculescu, C. Balan, V.C. Diculescu, An electrochemical DNA quantification sensor on chromatographic paper with attached electrodes from conductive electrospun polymeric fibers, *Advanced Materials**
2. **D. Botta**, M. Beregoi, A. Evanghelidis, A. Pascu, I. Enculescu, V.C. Diculescu, An impedimetric sensor on chromatographic paper with attached electrodes from conductive electrospun polymeric fibers for quantification of nucleic acids, *ACS Sensors**
3. **D. Botta**, A. Evanghelidis, E. Matei, I. Enculescu, V.C. Diculescu, A paper-based architecture with conductive electrospun polymeric fibers for wearable biosensors, *ACS Applied Materials and Interfaces**

* intended journal.

VII. Member of *International Society of Electrochemistry (ISE)* – since 2023.

Chapter 1. Introduction

From an industrial point of view, the applications of diffusion through porous materials can be found in areas such as: development of energy storage devices [1-3], catalysis of oxygen reduction or hydrogen evolution reactions as renewable energy sources [4,5], development of structures with high absorbance for greenhouse gas compounds capture from the atmosphere [6] or water purification [7,8], development of sensors for the detection of substances in complex fluids or gaseous compounds for monitoring air or water quality in order to optimise the operation of various installations.

The increased interest in porous materials is due to their structural properties, which allow both passive fluid transport under the action of capillary force, and efficient storage of chemical compounds in their structure by adsorption, due to their large contact surface.

In addition, the example of sweat diffusion in textiles has generated the nucleus around which the field of wearable sensors development has emerged, an additional advantage of these being their functionality with low voltage supply (1.5 V) [9]. Such sensors allow continuous monitoring of both health and environmental status, with low energy consumption compared to that required for a clinical analysis laboratory.

State of the art

The importance of portable sensors lies in the ability to monitor in real time the presence or absence of a chemical compound in the test medium. Point-of-care (PoC) devices have been defined in the literature as being devices which can be used "in close proximity to the patient, rather than in the traditional environment of a clinical laboratory" [10], to provide information about the health status of a patient. However, the fabrication methods and detection strategies used in PoC devices are also applicable for continuous environmental quality monitoring. Such analytical devices should be portable, easy to use, efficient to manufacture, and capable of being integrated with electronic circuits and batteries [11].

Electrochemical sensors with porous substrates could be applied in the biomedical field for the detection of different chemical compounds such as ions [12-15], small molecules [16-19], proteins [20-23] and nucleic acids [24-26]. Outside the biomedical field, their applications could be extended to the detection of contaminants in concrete [27], drugs [19,28] and pesticides on fruit peel [29], in soil [30] or aerosols [31], **Figure 1.1**. Fabrication techniques are constantly being evaluated and optimised, but few devices reach the commercial state, being mainly functional only under laboratory conditions.

Thus, in order to develop reliable devices with reproducible features and functionality, even outside a controlled environment, the most optimal architectures, paper modification strategies and hydrophobic barrier fabrication, as well as methods of integrating it with electrodes must be identified. The techniques and methods for the detection of different types of analytes should also be considered, taking into account transport and adsorption processes in porous media
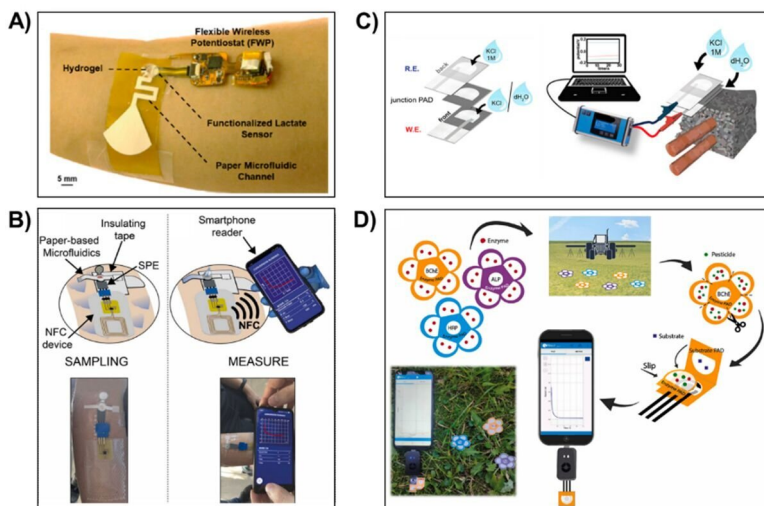
Figure 1.1. Examples of portable electrochemical sensors for monitoring: **A)** lactate in human sweat, reproduced from [16] with permission from the *American Chemical Society*, **B)** cortisol, reproduced from [32] with permission from *Elsevier*, **C)** contamination of concrete structures with chlorine ions, reproduced from [27] with permission from the *American Chemical Society*, **D)** pesticides, such as paraoxon and glyphosate, in the aerosol phase, reproduced from [31] with permission from *Elsevier*.

Aim and motivation

The first objective of this thesis was to study diffusion processes in porous media, taking the case of a droplet in contact with a paper substrate. The analysis was focused on studying the uniformity of the process and the diffusion velocity of the fluid front in the cases of radial and unidirectional wicking. The analysis was aimed at describing the influence of the material properties of the fluid on the process, thus fluids with different viscosities were included in the study, as well as solutions with molecules including chromophores in the chemical structure, for the study of the retention phenomenon.

A second objective of the thesis was to ease the diffusion analysis process, and for this purpose a numerical algorithm was implemented for the automatic processing of frames extracted from diffusion recordings. The algorithm was applied to study the correlation between diffusion through the porous medium and the evolution of the droplet interface remaining at the surface of the substrate.

The third objective of the thesis included the study of material and environmental parameters on the manufacturing process of fibrillar porous materials from polymer solutions. A comparison between fabricated surfaces and filter paper was performed and the optical and electrical properties of these materials were analysed.

The final aim of the thesis involved the integration of porous substrates with electrodes formed from polymeric meshes, for the development of wearable sensors. Different architectures were analysed and electrochemically characterised, in order to obtain optimal devices. Their functionality was demonstrated by performing electrochemical detection and quantification of analytes present in sweat, as well as nucleic acids.

Thesis structure

Chapter 1 presents the current state of studies regarding diffusion in porous media, as well as the current progress in the development of sensors based on porous substrates. The methods of fabricating and integrating the electrodes with porous substrates, as well as the methods involved in electrochemical detection have been reviewed.

Chapter 2 presents the theoretical description of the diffusion phenomenon in paper considering the unidirectional and radial cases. The evolution of the droplet interface for a fluid in contact with a porous medium is also discussed.

Chapter 3 discusses the experimental techniques used to carry out the experiments and describes the physical or chemical phenomena underlying the processes.

Chapter 4 presents the steps of the image processing algorithm developed, its method and limitations in interface identification, and the mathematical formalism used to calculate parameters such as diameter, volume, contact angle and diffusion velocity.

Chapter 5 is dedicated to the experimental study of the diffusion process in porous media. The cases of unidirectional diffusion in the presence of wax barriers, and radial, uninfluenced diffusion are analysed. In the case of unidirectional diffusion the influence of channel width was investigated. For the case of radial diffusion, the influence of viscosity on the diffusion velocity as well as concentration on the molecule retention phenomenon were studied. Finally, the diffusion of viscoelastic fluids was investigated by analyzing the evolution of the droplet interface over time.

In **Chapter 6**, two techniques for fabricating porous surfaces from polymer fibers are studied. The rheological characteristics of the polymer solutions and the environmental or process parameters influence on the fabrication processes was analysed. The characteristics of the polymer meshes were investigated in terms of morphology and wetting properties. Conductive layers were deposited on their surface and their electrical and electrochemical characteristics were studied.

Chapter 7 presents the procedure developed for fabricating an electrochemical sensor with a paper substrate and electrospun fiber mesh electrodes. Different types of architectures were analysed in terms of electrochemical behaviour, in order to identify the optimal configuration. Subsequently, this configuration was used for the detection of different chemical compounds, using amperometric, voltammetric and impedimetric techniques.

The conclusions of the thesis, original contributions to the field and future research perspectives are discussed in **Chapter 8**. The thesis concludes with eight appendices containing visualizations of impact phenomena, numerical codes for image processing and specifications of the experimental devices used.

Chapter 2. Theoretical Background

Introduction

Fluid wicking in porous media is defined as "the spontaneous transport of a fluid driven by capillary forces" [33]. Capillarity is the ability of a fluid to passively flow through a narrow space, even when upon it are acting forces of opposite direction relative to the motion (such as gravity). Porous materials such as paper or textiles are networks of fibers, between which capillary spaces (pores) are formed, saturated with gas, which is usually air. The porosity of such a material is defined as $\mathcal{P} = \frac{V_0}{V_t}$, where V_0 is the volume occupied by air (pore volume) and V_t is the total volume occupied by the porous medium. The absorption and diffusion processes are considerably influenced by the interfacial tension between fluid and fibers, the viscosity of the fluid and the capillary dimensions of the substrate. The process will also behave differently depending on the volume of fluid, thus being defined systems with infinite reservoirs (the case of a porous medium immersed in a filled container) or finite reservoirs (the case of a droplet deposited on the substrate).

While the phenomenon can be analysed from a parallel plane, observing the displacement of the fluid front over time, performing the study of the in the lateral plane offers the possibility to observe the evolution of the droplet remaining on the surface of the substrate as it is absorbed, being able to extract information such as the evolution of the: remaining volume, contact angle, droplet height and contact area, **Figure 2.1**.
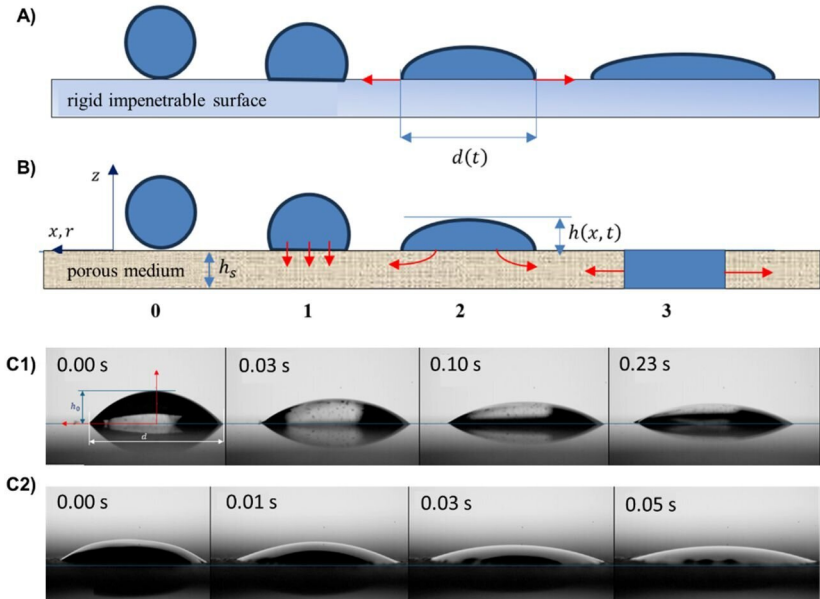

Figure 2.1 Dynamics of a liquid after droplet impact on **A)** a rigid impenetrable surface and **B)** a porous surface of thickness h_s: (0) droplet impact, (1) vertical diffusion, (2) radial-vertical diffusion, (3) radial diffusion. Visualizations of droplet evolutions on **C1)** glass and **C2)** paper (porous medium).

Flow through porous media

Flow in a homogeneous porous medium is described by the Darcy - Brinkman - Forchheimer equation:

$$grad\,p = -\frac{\eta}{\kappa}\boldsymbol{v}_p + \eta^*\Delta\boldsymbol{v}_p - \frac{\rho}{\kappa_1}|\boldsymbol{v}_p|\boldsymbol{v}_p, \qquad (2.1)$$

where the pressure gradient is determined by three components: (i) porosity (Darcy), (ii) viscous friction (Brinkman) and (iii) inertia (Forchheimer) [34–36]. In (2.1) $\boldsymbol{v}_p$ is the surface velocity in the porous medium (defined as the ratio of the fluid flow rate to the cross-sectional area in the porous substrate), κ is the permeability of the medium (which is porosity dependent), η is the fluid viscosity (assumed Newtonian), η^* the effective viscosity of the fluid flowing through the porous medium, κ_1 is the inertial permeability and ρ the fluid density. For the particular case where $\eta^* = 0$ and $\kappa_1 \to \infty$, the relation (2.1) for a non-isotropic/neomogeneous medium becomes:

$$\boldsymbol{v}_p = -\frac{1}{\eta}\,\mathbf{K}\cdot grad\,p \qquad (2.2)$$

where $\mathbf{K}$ is a second order tensor [34,37]. In this case the permeability depends on the direction of flow.

For a homogeneous and isotropic medium, the permeability is a scalar, (2.2) becoming the classical Darcy's relation, [38]:

$$\boldsymbol{v}_p = -\,M\,grad\,p \qquad (2.3)$$

where $M := \frac{\kappa}{\eta}$ is the fluid mobility through the porous medium.

It should be noted that permeability does not depend exclusively on the porosity of the medium. The hydrophobic or hydrophilic character of the porous structure in relation to the fluid also has a strong influence on permeability.

Droplet flow on smooth and porous surfaces

In the case a viscous fluid droplet moving on a rigid (porous or impermeable) surface, **Figure 2.2**, under the assumption of Stokes flow (in which pressure forces are balanced by viscous frictional forces) and under the assumption $h(x,t) \ll d$, the deformation of the free surface is described by the thin film equation (a particular solution of the Navier-Stokes equation).
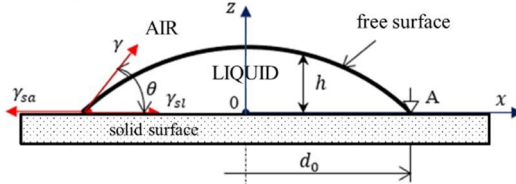

Figure 2.2. The position of a viscous liquid droplet on a solid surface and the linear force balance at the contact point. In the dynamic case, the geometrical quantities are time dependent: contact angle θ^o, wetting length/diameter d_0 and height h. For a given fluid, $\theta^o < 90°$ defines a hydrophilic surface, $\theta^o > 90°$ defines a hydrophobic surface.

In the case of interface displacement along the wall (i.e. contact point A) on the solid surface: $\gamma_{sa} > \gamma_{sl} + \gamma \cdot cos\theta$ [39]. At time t = 0 (onset of the motion) the configuration shown in **Figure 2.2** is considered known, the equation of the free surface (of the interface) being: $h = h(x,0)$.

Considering the reference quantities: $d_{00} := d_{0,t=0}$, for lengths and $t_0 := d_{00}/v$ for time, with $v := \gamma/\eta$ [m/s] the capillary velocity, it follows that $t_0 v/d_{00} = 1$. The evolution of the interface at the surface of the porous medium will be described by the dimensionless relation:

$$\frac{\partial h}{\partial t} = \mathcal{D}a\left(\frac{\partial^2 h}{\partial x^2} - \mathcal{B}o h\right) - \mathcal{N}a\frac{\partial h}{\partial x}\frac{\partial^3 h}{\partial x^3} \qquad (2.4)$$

8

where $\mathcal{D}a = \mu/d_{00}$ is the linear Darcy number, $\mathcal{N}a = \alpha/3d_{00}^2$ the Navier number at the interface and $\mathcal{B}o = \frac{\rho g d_0^2}{\gamma}$ the Bond number. Dimensionless equations similar to (2.4) are obtained by Davis & Hocking in [40]:

a) Porous wall flow only in vertical direction (no slip) for $R_0 \gg h_0$:

$$\frac{\partial h}{\partial t} = k \left(\frac{\partial^2 h}{\partial x^2} - \mathcal{B}o \cdot h \right) \tag{2.5}$$

with the solution $h = \frac{V_0 e^{-k\mathcal{B}o t}}{2\sqrt{\pi k t}} e^{-x^2/4kt}$, where at $t = 0$: V_0 is the initial volume, R_0 and h_0 the radius and the maximum height of the interface at $z = 0$, these also definining the characteristic lengths in the two directions. In the dimensioning process the following characteristic quantities were used: $t_0 = \frac{3\eta R_0}{\gamma} \left(\frac{R_0}{h_0} \right)^3$ for time, $k_0 = \frac{1}{3} \left(\frac{h_0}{R_0} \right)^3 R_0$ for the linear permittivity k [m], with $\mathcal{B}o = \frac{\rho g R_0^2}{\gamma}$.

b) Porous wall flow in both directions; for $k\varphi \mathcal{B}o t \gg \delta$:

$$\frac{\partial h}{\partial t} = K \frac{\partial^2 h}{\partial x^2} \tag{2.6}$$

where $K = k \, \varphi \, \mathcal{B}o \, \delta$ (φ is the porosity and δ is the thickness of the porous substrate), with the solution $h = \frac{V_0}{2\sqrt{\pi K t}} e^{-x^2/4Kt}$. In the expression of the coefficient K in (2.6) the permittivity k[m^2] is dimensionless with $k_0 = \frac{1}{3}\frac{h_0^3}{R_0}$. It is important to note that the expressions (2.4), (2.5) and (2.6) are approximations of the equation describing the droplet dynamics for $h \ll d$, thus in the second phase of the diffusion process on the porous surface. The numerical solutions of equations (2.5) and (2.6), obtained in *Mathematica*, are shown in **Figures 2.3 - 2.4**. The initial condition imposed for $t = 0$ is $h = \sqrt{1 - x^2}$, for $x \in [-1,1]$, **Figure 2.3**, the boundary condition being $h(t) = 0$ at $x = \pm 10$ (approximation condition: $x \to \infty$).
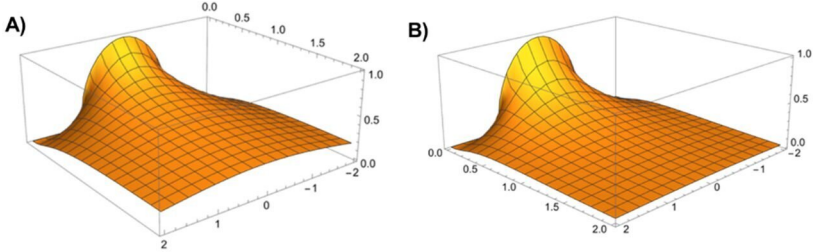

Figure 2.3 Fluid height variation $h(x,t)$ – numerical solutions: **A)** diffusion equation (2.6), $K = 1$; **B)** modified diffusion equation (2.5), $k = 1$, $\mathcal{B}o = 1$ (initial condition: $h(x, 0) = (1 - x^2)^{0.5}$ (UnitStep$[x + 1]$ − UnitStep$[x - 1]$).
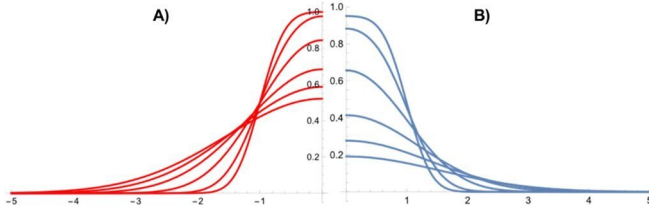

Figure 2.4 Evolution of $h(x)$ for $t = 0.05, 0.1, 0.25, 0.5, 0.75, 1.0$, taken from **Figure 2.3**.

It was observed that the presence of the term proportional to the Bond number in (2.5) leads to a faster diffusion process, but does not bring qualitative changes in the height distribution.

Radial diffusion of a drop in porous media

In the third phase of the diffusion process, $h \cong 0$, the droplet is completely absorbed into the porous medium, in which case the diffusion occurs exclusively in the radial direction. A variant of the radial diffusion equations, in which the unknown term is the volume concentration of the liquid in the porous medium $\mathcal{C}$, was obtained by Gillespie [41] and later by Borhan&Rungta [42,43]. Starting from Darcy's equation (2.3) and considering the concentration proportional to the relative density of the liquid in the porous medium, the continuity relation with source term (given by the time variation of the liquid concentration in the porous medium, similar to the density variation in the case of compressible media) becomes [41]:

$$\frac{\partial \mathcal{C}}{\partial t} = div\left(-\frac{\kappa}{\eta} gradp\right), \tag{2.7}$$

equivalent to:

$$\frac{\partial \mathcal{C}}{\partial t} = -\frac{\beta}{r}\frac{\partial \mathcal{C}^3}{\partial r} \tag{2.8}$$

with the conditions: $\mathcal{C} = \mathcal{C}_s$ (saturation concentration) at $t = 0$ and $r = 0$; $\mathcal{C} = 0$ for $r = R$ when $t > 0$ in the Gillespie hypothesis [65], or

$$\frac{\partial \mathcal{C}}{\partial t} = \frac{\alpha}{r}\frac{\partial}{\partial r}\left(r\mathcal{C}^n \frac{\partial \mathcal{C}}{\partial r}\right) \tag{2.9}$$

with the conditions: $\mathcal{C} = 1$ at $t = 0$ and $r \leq 1$; $\mathcal{C} = 0$ for $r = R$ and $\frac{\partial \mathcal{C}}{\partial r} = 0$ for $r = 0$ when $t > 0$, in the Borhan&Rungta hypothesis [42]. In (2.8) and (2.9) β and α are constants and $R(t)$ is the radius of the wetted porous surface of thickness h_s. Imposing a semi-empirical dependence between the concentration change $\mathcal{C}(r,t)$, the pressure gradient and the time variation of the radius $R(t)$, given an approximate solution of equation (2.9) and the fluid volume conservation equation,

$$V_0 = 2\pi h_s \int_0^{R(t)} \mathcal{C}(r,t)rdr \tag{2.10}$$

in [42] a description for R is proposed as:

$$R(t) = R_0 \left[1 + \left(\frac{4(n+1)\alpha\gamma\kappa}{n\eta R_0^2 h}\right)t\right]^{1/2(n+1)} \tag{2.11}$$

or in dimensionless form,

$$\overline{R(t)} = \left(1 + a\frac{4(n+1)}{n}\bar{t}\right)^{1/2(n+1)} \tag{2.12}$$

with $\bar{R} = R/R_0$, $\bar{t} = t/\left(\frac{\eta h_s}{\gamma}\right)$ and $a = \alpha\kappa/R_0^2$. The variation of the radius $R(t,n)$ in (2.11) is plotted in **Figure 2.5 A)**, for a fixed value of the coefficient a. The semi-empirical relation (2.9) is also based on the strongly non-linear diffusion equation. Even in this case, the solution (2.12), especially in the 3rd phase of the diffusion, follows the evolution predicted by the solutions of the simplified equations (2.5) and (2.6), **Figure 2.5 B)**.

Since the numerical solutions of the nonlinear equations modelling droplet diffusion in a porous medium are difficult to obtain (mainly due to insufficient knowledge of initial and boundary conditions), in practice, the variation of the wetted dimeter in time can be described by power functions such as Borhan&Rungta (2.11) or exponential functions:

$$y(t) = e^{a+\frac{b}{x+c}} \tag{2.13}$$

or logistic:

$$y(t) = \frac{a}{1+e^{-k(x-x_0)}} \tag{2.14}$$

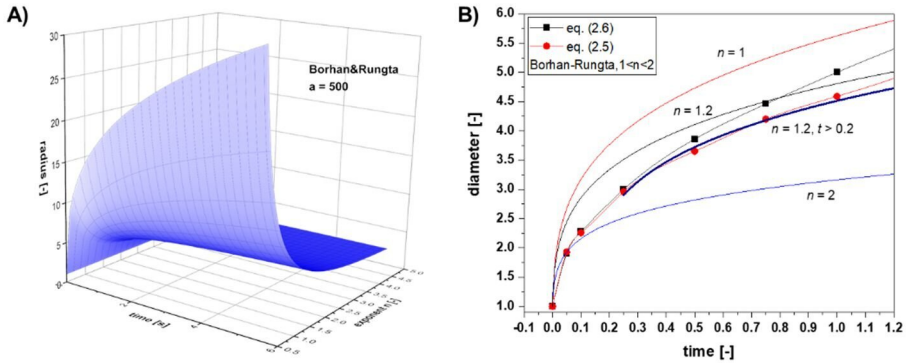represented in **Figure 2.6**.

A)

B)

Figure 2.5 A) Representation of the relation (2.11) for exponent values $n \in [0.5 \div 4]$, in the time interval $0 \le t \le 5$. **B)** Variation of the wetted diameter extracted from the numerical solutions, **Figure 2.6**, corresponding to the value h=0.002; comparison with the solution proposed by Borhan&Rungta (2.12).
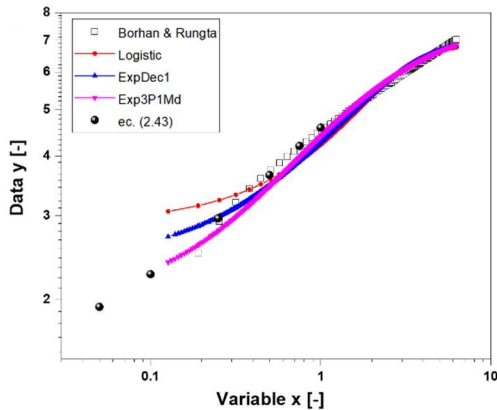

Figure 2.6 Exponential and logistic functions used for modelling the time variation of wetted diameter in a porous medium. Variation of the model (2.12) and the solution of the diffusion equation are also shown.

    In conclusion, it can be considered that the phenomenon studied in this thesis, the flow of a viscous liquid in a porous paper substrate, is qualitatively modelled by the diffusion equation. The real phenomenon is nonlinear, so the numerical solutions presented cannot represent the flow satisfactorily and quantitatively. Since the visualization of the flow is mainly obtained in 2nd and 3rd phases of the diffusion, the formulas (2.11) and (2.12) will be used in the analysis of the diffusion process of liquids in the porous substrate, as they satisfactorily model the variation in time of the wetted diameter [44].

Chapter 3. Experimental Procedures

Electrospinning and rotary-jet spinning techniques were used to fabricate porous materials with a fibrillar structure from polymer solutions, under the action of electrostatic force and centrifugal force respectively, **Figure 3.1**. Subsequently, the conductivity of these structures was ensured by depositing thin metal layers by magnetron sputtering. The morphological characterization of the resulting materials was performed by scanning electron microscopy. The acquired results are presented in **Chapter 6**.

The study of fluid diffusion in porous media was performed by image analysis. For this purpose a numerical image processing algorithm was developed in MATLAB, described in **Chapter 4**.

Molecular interactions in the porous substrate were investigated by spectroscopic techniques such as UV-Vis-NIR spectrophotometry and Raman spectroscopy. The applicability of porous media was investigated by assembling an electrochemical cell based on conductive structures of polymer fibers and paper substrate. The characterization of the electrochemical cell and the proof-of-concept were performed by electrochemical techniques, and the obtained results are described in **Chapter 7**.
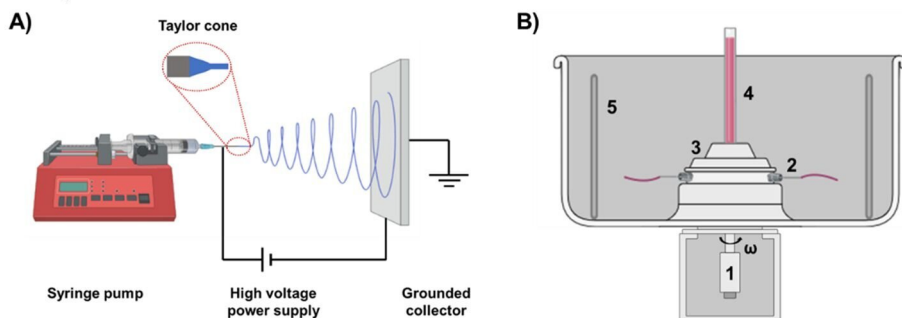

Figure 3.1. A) Scheme of the experimental set-up for the fabrication of electrospun fibres. **B)** Scheme of the experimental device for centrifugation and its components, **1)** motor for printing the speed, **2)** capillary orifices, **3)** tank, **4)** tube for injecting the polymer solution into the tank, **5)** bars for collecting the fibers.

Chapter 4. Automated Imaging Analysis Procedure for Diffusion Analysis

The diffusion process in porous media is usually analysed by digitally recording the phenomenon and extracting information from single frames. However, since the phenomenon occurs very fast, it is necessary to use high-speed cameras, resulting in a large amount of frames to analyse. In order to make the diffusion study more efficient, a numerical code has been developed, which can be used to analyse both the evolution of the droplet shape and the diffusion of the fluid front. The advantage of this method lies in the possibility to study not only static droplets, but also those whose interfaces change over time. Compared to other techniques, knowledge of the fluid properties is not necessary, as all parameters will be calculated from the droplet shape. Moreover, the proposed code can easily detect the interfaces of colourless fluids, thus eliminating the need to use dyes, which could influence the surface tension of the fluid. In the case of diffusion analysis performed from the lateral plane, the purpose of the code is to identify the droplet interface and calculate parameters such as diameter, volume and contact angle. The experimental measurements were performed with solutions of poly(ethylene oxide) (PEO) of low concentrations, this type of fluid being chosen because of its weak viscous and elastic behaviour. By varying the concentration, the resulting fluids can represent models for a wide range of fluids of interest in terms of their behaviour.

Measuring procedure

PEO solutions were prepared in water with two concentrations: 0.5% and 5% (w/v). Droplets with volumes between 1 and 2 µl were placed on the paper surface and the diffusion was recorded in the lateral plane. To ensure high image quality with low noise, the paper was illuminated from two positions: one light source was placed behind the droplet and the other under the paper, **Figure 4.1**.
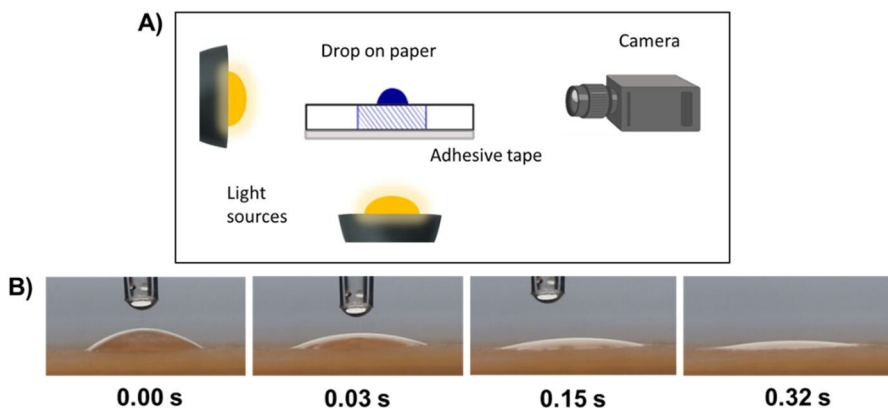

Figure 4.1. **A)** Experimental setup for recording drop wicking in paper. **B)** Frames extracted from the recording of a PEO droplet wicking on paper substrate.

Numerical code algorithm for interface analysis

The code is designed so that it can retrieve RGB images, which are converted to grayscale and then to binary, **Figure 4.2**. The binarization threshold was kept the same ($x > 151$) for all images analyzed in this study. In order to extract the interface between the fluid and the surrounding air, a for-loop was performed on the binary matrix, which identifies the first non-zero

element (white pixel) in each column. For each element, its position on the rows and columns was stored in two vectors, thus containing the coordinates on the OX and OY axes for each point of the interface. By multiplying the two vectors with a scaling factor, the information is converted from pixels to mm. The interface is then centered on $X = 0$ by translating the vector corresponding to the X-axis coordinates. Finally the interface points are interpolated with a 7th degree polynomial function.
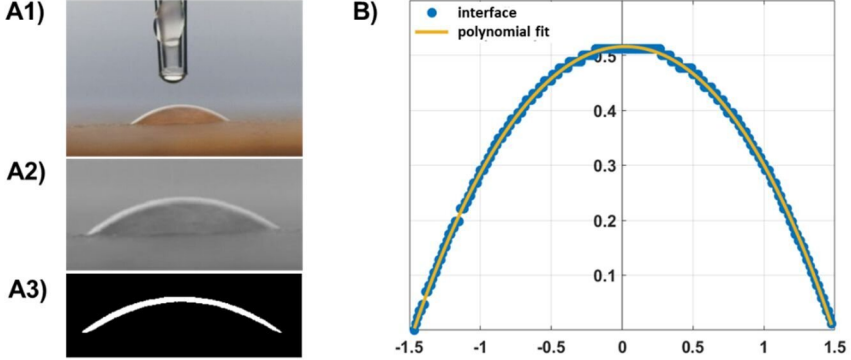

Figure 4.2. The steps performed by the numerical code: **A1)** retrieval of the original image in RGB format, **A2)** conversion to grayscale, **A3)** conversion to binary and identification of the first non-zero element for each column, **B)** representation of the interface points fitted with a 7th degree polynomial function.

With the interface represented as such, the height can be determined as $h = f(0)$, and the radius of the drop, r, is the absolute value of the X-axis coordinate of the last point of the interface. The diameter will be calculated as $D = 2r$, and the volume of the droplet can be approximated as the solid of revolution around the Y-axis:

$$V(x) = 2\pi \int_0^r x \cdot f(x)\, dx. \tag{4.1}$$

In order to determine the contact angle, the first 30 points of the interface are subsequently interpolated with a linear function and its value is obtained as the arctangent of the slope:

$$\theta = \tan^{-1} f'(x). \tag{4.2}$$

The analysis of the interface evolution over time was performed in a for loop, which ran for each frame found in the specified directory, and the values for frame number, diameter, volume and contact angle were saved in corresponding vectors. The vector representing the frame numbers was scaled to seconds by multiplying with a correction factor, corresponding to the recording speed. Diffusion velocity and flow rate were calculated as the absolute values of the first-order derivatives of the diameter, $v = |dD/dt|$, and volume, $Q = |dV/dt|$, respectively.

Evaluation of interface detection error

The accuracy in interface representation depends directly on the binarization threshold used. The interface detection error was calculated by analyzing the grayscale image and identifying the number of pixels corresponding to the border between background and drop. The average distance between the first non-zero element and the one whose value is less than half of the neighbouring

pixel was identified as 3 pixels, **Figure 4.3**. In the analysed case, the metric equivalent of a single pixel is 0.0116 mm, therefore the measurement error was considered 0.034 mm.
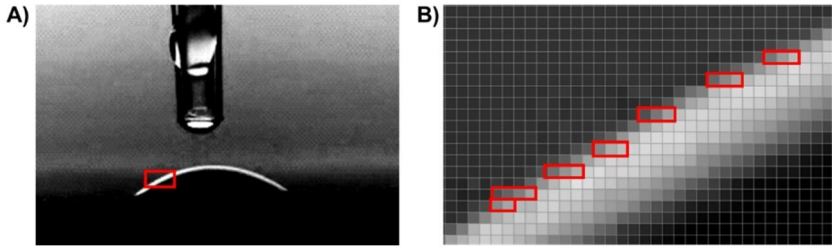

Figure 4.3 A) Representation of the greyscale image and the area chosen for assessing the boundary between the drop and the background. **B)** Enlarged view of the interface and the pixels considered to correspond to the boundary.

Application of the code in droplet diffusion analysis

In the first step the interface was detected and its evolution over time was represented, **Figure 4.4**. For each frame the contact angle, height, diameter, area and volume were evaluated according to the procedure described above, **Figure 4.5**. The fitting of the experimental points was performed with smooth functions for diameter and exponential functions for contact angle and volume.
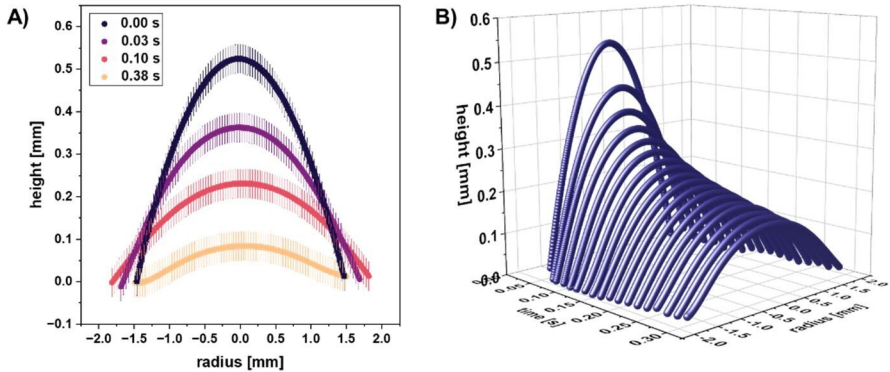

Figure 4.4. Evolution over time of the interface detected by numerical code, plotted in **A)** 2D and **B)** 3D.

For the analysed case, the measurement error had a strong impact on the accuracy of the drop height representation, but does not significantly influence the dimeter evaluation. The choice of the fitting function for the diameter points is of utmost importance, as this will have a major impact on how the derivative is represented. Although the experimental points could have been interpolated with a 2nd degree polynomial function, this would have resulted in the velocity being represented as a linear function over the entire time interval. Fitting with a smooth function allows for calculus of the derivative with higher accuracy in respect to the experimental points.
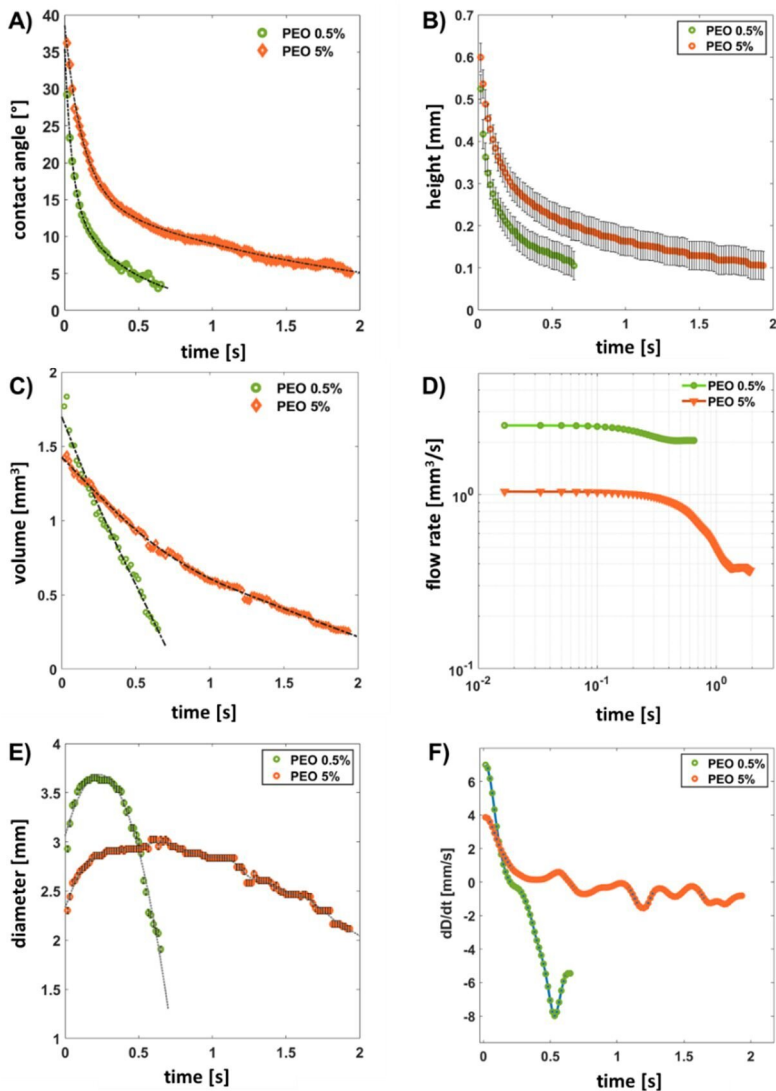
Figure 4.5. Evolution over time of the parameters calculated from the droplet interface: **A)** contact angle, **B)** height, **C)** volume, **D)** flow, **E)** diameter and **F)** 1st order derivative of diameter.

The applicability of the numerical code for the study of diffusion in porous media was thus demonstrated, and the average run time was 0.75 seconds per frame. For the cases investigated, the absorption phenomenon of a single droplet could be analyzed in about 1 minute. Thus, the numerical code can be used to better understand how the material properties of the fluids influence the diffusion process, in particular the velocity of the fluid front.

Chapter 5. Experimental Study of the Diffusion Process in Paper

Unidirectional diffusion in the presence of hydrophobic barriers

The unidirectional diffusion study was performed using a filter paper of 0.2 mm thickness as porous medium. To restrict fluid flow in one direction, hydrophobic barriers were created on the paper surface by wax printing. Wax penetration deep into the paper was ensured by heat treatment.

In order to understand how wax barriers affect fluid diffusion, the morphology of the filter paper was investigated before and after wax printing, as well as before and after heat treatment, **Figure 5.1**. It was observed that although wax printing involves coating the porous surface with a solid pore-blocking material, **Figure 5.1 B1)**, after heat treatment, the morphology of the modified paper is very similar to the unmodified one, **Figure 5.1 A1)**. However, the surface of cellulose fibers presented a higher roughness in the unmodified state, **Figure 5.1 A2)**, compared to the ones modified with wax and heat-treated, **Figure 5.1 C2)**.
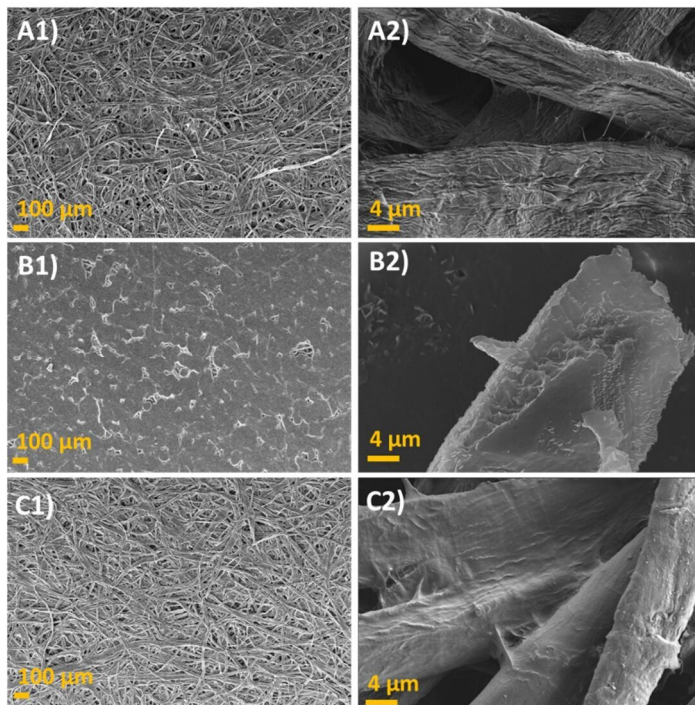
Figure 5.1. Filter paper morphology **A)** in unmodified state, **B)** after wax printing, **C)** after heat treatment of the deposited wax.

The hydrophobicity of the deposited layer was investigated using drops of 2 µl 1% (w/v) methylene blue (MB) prepared in ultrapure water, placed on the heat-treated wax-modified paper, **Figure 5.2**. It was observed in this case that hydrophobicity can be achieved by printing the paper with two layers of wax. Taking into account the results obtained by electron microscopy and the measured contact angles, it was considered that the hydrophobicity of the wax-modified paper is

not due to pore blocking, but to a surface modification of the cellulose fibers. As wax is a water-insoluble lipid molecule, both the chemical properties of the wax covering the surface of the fibers, and the roughness of the fibers' surface can influence the interfacial tension between the fluid and the porous medium.
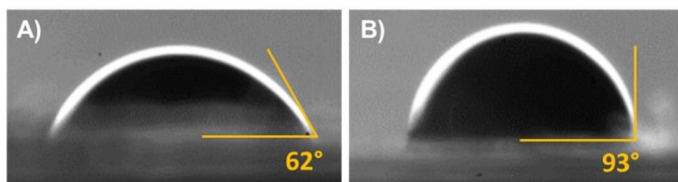

Figure 5.2. The contact angle between a drop of MB and paper modified with **A)** one layer of wax and **B)** two layers of wax.

Subsequently, channels with varying distances between the two wax barriers were designed to investigate the influence of channel width on diffusion, **Figure 5.3 A)**. The study was carried out by pipetting MB droplets with volumes of 5 µl into the channel and the fluid diffusion was recorded at a rate of 8000 frames per second. The analysis procedure consisted of measuring the distance between the fluid front and the initial position at $t = 0$, **Figure 5.3 B)**. In order to observe whether the diffusion is uniform across the channel width, the variation of the distance over time was measured on three directions of interest. The results obtained were averaged and fitted with a 4th degree polynomial function, **Figure 5.4**. The interpolation curve was derived with respect to time, to obtain the fluid velocity variation and it was represented along with the numerical derivation of the experimental points.
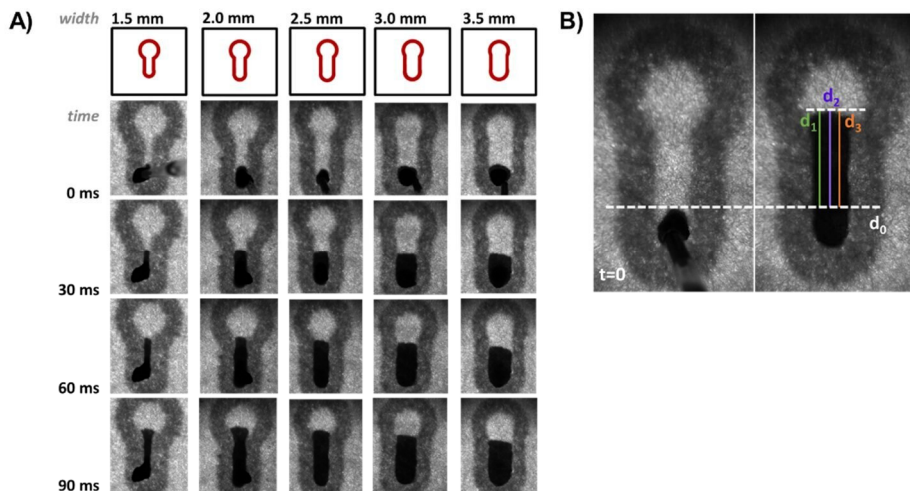

Figure 5.3. **A)** Vector diagrams for the fluidic channels variable widths, and the frames extracted from diffusion recordings of a 5 µl MB droplet. **B)** Schematic of the measurement method: initial position of the fluid front and the three directions considered for the measurements.
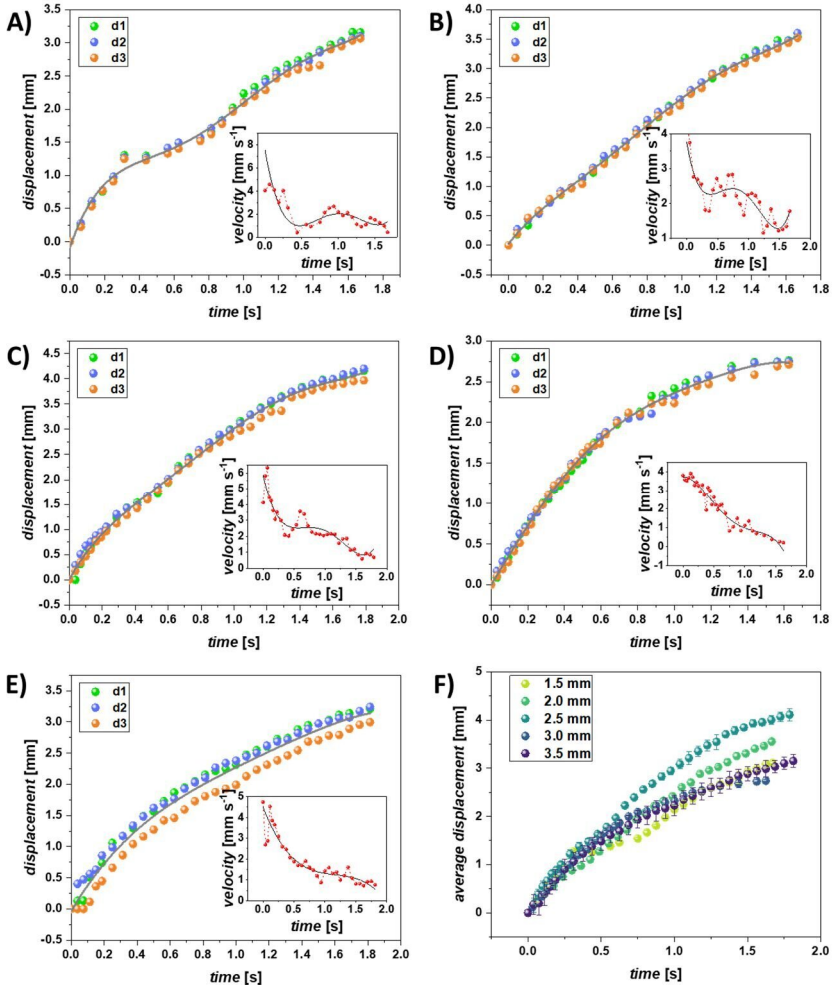
Figure 5.4. Variation over time of the fluid front displacement evaluated in three directions of measurement, for channels width of: **A)** 1.5 mm, **B)** 2.0 mm, **C)** 2.5 mm, **D)** 3.0 mm, **E)** 3.5 mm. **F)** The average displacement obtained for each channel width. Insets: Diffusion velocity evolution represented as the first-order derivative of the interpolation curve (black) and experimental points (red).

It was observed that the diffusion phenomenon did not occur at a constant speed along the length of the channel. The diffusion velocity reached a maximum immediately after the droplet came into contact with the paper surface, following a slow decrease until the end of the process. Two flow regimes were identified for each investigated channel, characterized by inflection points in the evolution of the front displacement over time and local minima in the velocity evolution. These regimes were attributed to the initial phase of droplet expansion on the substrate surface and to the absorption phase in the porous medium.

In narrow channels, the local velocity minima are more pronounced. This phenomenon can be explained by the pressure difference between the fluid and the gas that completely saturates the pore medium at the beginning of the process, which is localised over the entire contact surface between the droplet and the substrate. As the fluid diffuses, the capillary force will act on a much smaller area near the fluid front. In addition, being a finite reservoir, during the diffusion process, the volume available at the paper surface is consumed until the diffusion occurs only through the pores of the paper, further limiting the area on which the capillary force acts.

Velocity fluctuations during the process were attributed to the inhomogeneity of the porous medium. Thus, if the fluid front will encounter a region of the paper where the pore density is higher, the velocity will reach a local maximum. Similarly, if it encounters an area where the fibers are more condensed, some of the fluid will be absorbed into the fibres, causing swelling, thus reducing the forward motion of the fluid front.

In the case of wide channels, the way the fluid is brought into contact with the porous medium will have an influence on the diffusion until the end of the process. This is evident in the case of the 3.5 mm diameter channel, for which the fluid front is not axially symmetric at the end of diffusion, but this non-uniformity is present from the very beginning. As the placement is performed with a pipette, the evolution of the displacements will be influenced also by the moment of detachment of the droplet from the pipette tip. Thus, the inflection points observed in the velocity variation through the narrow width channels can also be attributed to the influence of an opposing force acting on the droplet when the pipette tip is withdrawn from the paper surface.

The influence of viscosity on radial diffusion

In a preliminary study, the radial diffusion was analysed in terms of process uniformity. For this purpose, a 1% (w/v) MB droplet with a volume of 2 µl was placed on the surface of the filter paper and allowed to diffuse freely, the displacement of the fluid front being measured in eight main directions, **Figure 5.5 A)**.

It was experimentally observed that the distance travelled by the fluid varied exponentially with time, diffusion being faster at the beginning of the process. Also, the phenomenon did not present uniformity, as the fluid front travelled a greater distance along the *d7* direction. Similar to the results obtained for unidirectional diffusion, this non-uniformity was attributed both to the inhomogeneity of the porous medium and to the influence of the pipetting method. In addition, since the volume of fluid was not restricted, influences such as inclinations of the plane could lead to a non-uniform diffusion. The fitting was perfomed with eq. (2.13) for the the results obtained on the *d7* and *d1* directions, **Figure 5.5 B)**. The constants of the equation were identified as: a∈[0.84,1.09], b∈[-0.047,-0.045] and c∈[0.023,0.030]. The initial diffusion velocity was obtained to be in the range [22,33] mm s^{-1}.

In the second step, droplets of equal volumes (2 µl) of fluids with different viscosities were allowed to diffuse radially, the objective being to analyse the influence of viscosity on the diffusion velocity. The study included six fluids with different material properties: deionised water, acetone, isopropanol, glycerol, sunflower oil and silicone oil. Since filter paper does not have a constant mean pore radius and the results obtained for MB showed non-uniformities in the diffusion process, all eight measurement directions were kept in the analysis of fluids with different viscosities, **Figures 5.6 - 5.7**. The experimental results for the fluid front displacement were fitted using the Borhan&Rungta model, eq. (2.11). As α and n are not imposed or tabulated values in the literature, the study aimed to find the values that provide a high degree of accuracy between the interpolation curve and the experimental data, **Figure 5.8**.
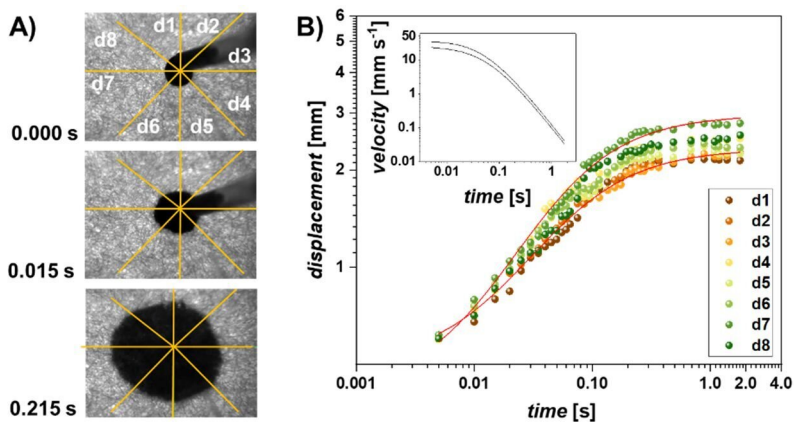
Figure 5.6. **A)** Radial diffusion of an MB droplet on paper and the directions considered for the measurements. **B)** Variation of the distance travelled by the fluid front over time fitted with eq. (2.13). Inset: Displacement velocity evaluated as the first order derivative of the fitted curve.

Figure 5.7. Radial diffusion on paper of **A)** deionized water, **B)** acetone, **C)** isopropyl alcohol. Recording speed: 10000 frames per second.

Figure 5.8. Radial diffusion on paper of **A)** silicone oil, **B)** sunflower oil, **C)** glycerol. Recording speed: 250 frames per second.
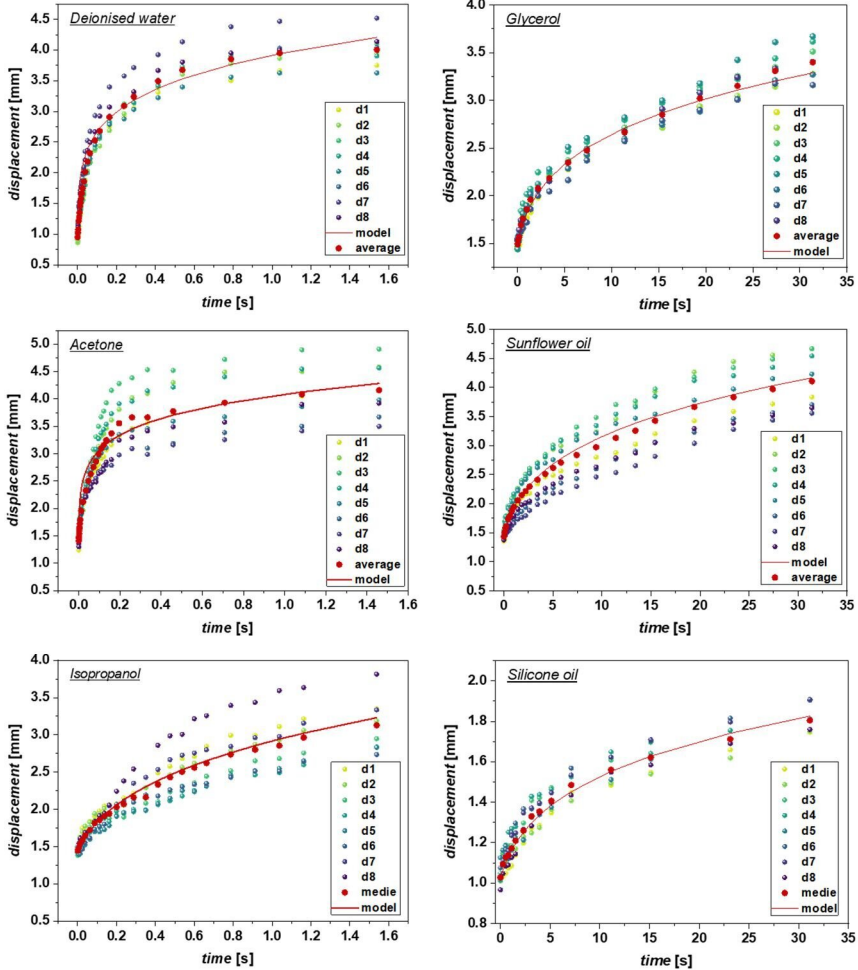
Figure 5.9. Displacement of the fluid front along the eight measurement directions for deionized water, acetone, isopropanol, sunflower oil, glycerol and silicone oil. Mean values were fitted with the Borhan & Rungta model.

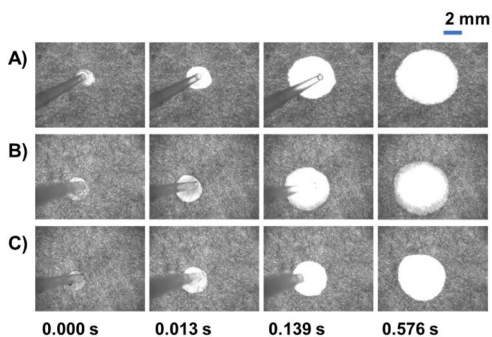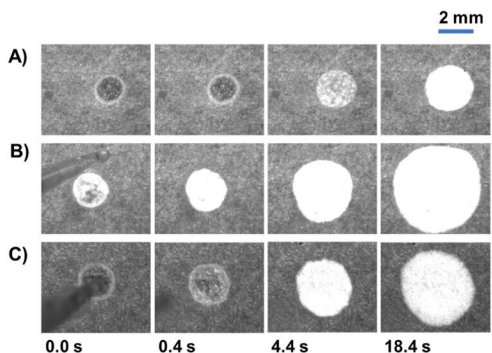Previous studies of radial diffusion reported a dependence $r \sim t^{\frac{1}{6}}$. This implies that $n = 2$ in Borhan & Rungta's law. Furthermore, in general, α is considered a material constant, so its value should vary only if the porous substrate is different. However, it was observed that $n = 2$ did not always provide the best fit, and changing the constant n also required a variation of α. The values determined for the two constants that led to accurate fitting curves in respect to the experimental results are presented in **Table 5.1**. The most accurate fits were obtained for isopropanol and the high viscosity fluids. In the case of deionised water and acetone, inconsistencies in the description of the initial diffusion phase were observed.

Tabelul 5.1. Experimentally determined values for the Borhan&Rungta's model constants, n and α.

Fluid	n	α
Deionised water	2	0.15
Acetone	3	0.4
Isopropanol	1	0.006
Sunflower oil	1	0.015
Glycerol	1.55	0.1
Silicone oil	2	0.15

For each fluid, the diffusion velocity was evaluated by calculating the first derivative of the displacement over time. For all fluids, the highest velocity was obtained at the onset of the process, with an exponential decrease thereafter. The highest value was obtained for acetone (80 mm/s) and the lowest for silicone oil (0.1 mm/s). Taking into account the material properties of the fluids, a dependence between the initial diffusion velocity and the viscosity was observed, **Figure 5.10**. The experimental points were fitted with a power function, $v_{max}(\eta) = a\,\eta^b$, the values for a and b being 27.6 and -0.88 respectively.
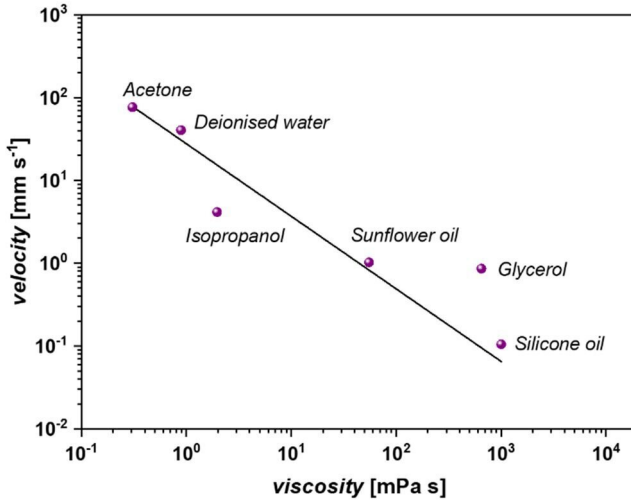
Figure 5.10. The dependence of inial diffusion velocity on viscosity.

In the case of isopropanol and glycerol, the deviation from the law could be attributed to effects not included in this study, such as the influence of environmental factors (humidity and temperature) or other material properties (surface tension or viscoelastic behaviour in the case of glycerol).

The influence of concentration for solvent-solute fluids

Fluids of biological interest or with biomedical applications are always complex systems of molecules (solute) dissolved in a liquid phase (solvent). When brought into contact with the

porous medium, the two phases tend to separate during the diffusion process. If the porous medium is a fibrillar substrate (made of cellulose in the case of paper), the diffusion processes of complex fluids cannot be understood only by studying the physical interactions. Cellulose is a natural polymer of the polysaccharide group, composed of glucose molecules and glycosidic bonds. Phase separation in paper occurs through the formation of hydrogen bonds between the molecules in the aqueous phase and hydroxyl groups in the cellulose fibre structure. Therefore, the separation process is influenced by the chemical properties of all the three materials involved (porous medium, solvent, solute), the important parameters being the polarity of the molecules and solvent, and the availability of hydrogen bonds in the structure of the pore medium. Therefore, analysis of the behaviour of a single chemical compound cannot provide general information applicable to all molecules, regardless of their dimension.

Retention phenomena were analysed by investigating diffusion in filter paper of solvent-solute systems, where the liquid phase is water, and the molecules included in the study were MB, gentian violet (GV) and fluorescein. Diffusion and separation processes were analysed for solutions with concentrations ranging from 10 µM to 10000 µM, **Figure 5.11 A)**.

In a first step, the influence of the molecules' presence on solvent diffusion was analysed. It was experimentally observed that for all concentrations used in this study, the solvent always reached a higher distance than the solute. Also, regardless of the type of molecule or the concentration of the solution, the solvent interface advanced into the porous substrate by similar distances, **Figure 5.11 B)**.
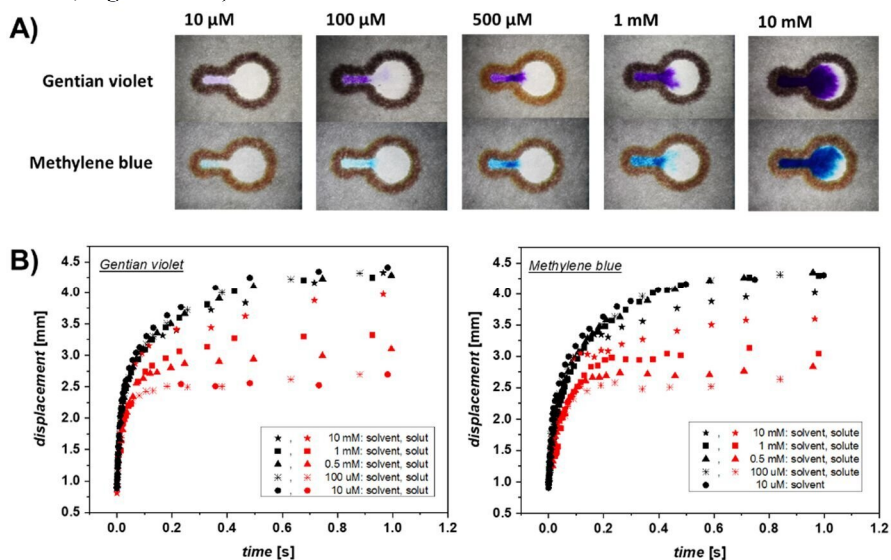
Figure 5.11. A) Diffusion in paper of solutions with different concentrations of GV and MB dissolved in water. **B)** Displacement of the fluid fronts associated with the solvent and solute phases, for GV and MB solutions with concentrations of (10, 100, 500, 1000 10000) µM.

In the case of the molecule diffusion, GV travelled longer distances in the paper substrate than MB. It was noted that the difference between the final distances reached by solvent and solute varies with the concentration of the solution. Thus, the smaller the quantity of dissolved molecules, the stronger the separation process will be evidenced, most of the molecules binding

to the cellulose fibers from the initial stages of diffusion. This led to the conclusion that the dissolved molecules in a solution will adhere to the paper substrate until local saturation occurs, and the front associated with the solute phase will only advance if there are free molecules remaining in the solution. It should be noted, however, that the velocity of the fluid can influence the retention process. Thus, if the fluid moves through the porous substrate at a velocity higher than the reaction rate for the bond formation between the dissolved molecules and the cellulose fibers, a higher concentration of molecules will remain in the aqueous phase, travelling longer distances. However, in this case, the fluid velocity must be externally stimulated (e.g. by using pumps). For each solution, the difference between the final distance reached by the solvent and solute was calculated and plotted on a line-log plot as a function of concentration, **Figure 5.12**. The variation trend was approximated by the function $\Delta(C) = -m \log_{10}(C) + b$, and the values obtained for m and b were 0.50 and 0.99 for GV, and 0.63 and 1.24 for MB respectively.
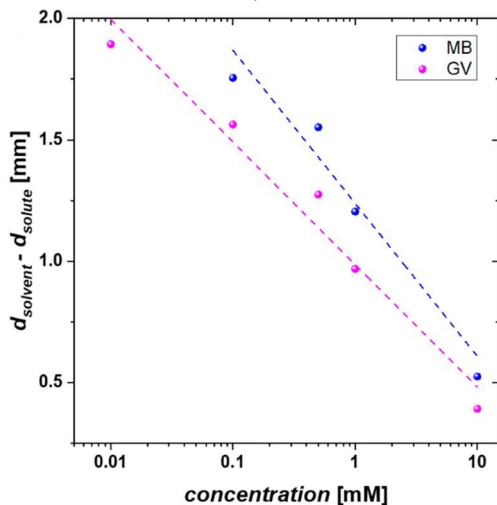
Figure 5.12. The difference between the final distances reached by solvent and solute plotted as a function of solution concentration.

In the second stage of the study, a method for approximating the solution concentration along the channel was implemented. For this purpose a 0.5 mM fluorescein solution was used, whose diffusion in the channel was recorded under UV irradiation, **Figure 5.13**. The approximation method is based on the assumption that a higher density of fluorescein molecules will emit a radiation of higher intensity. Therefore, analysis of the colour intensity could provide information about the concentration gradient along the channel.

Figure 5.13 Diffusion of 0.5 mM fluorescein.

The colour intensity histogram from each frame was extracted along the channel midline. The data was 3D plotted, **Figure 5.14 A)**, representing the colour intensity (in arbitrary units) as a function of distance along the channel, and over time. From these 3D plots, the background noise was subtracted so that the colour intensity would be zero in regions where fluorescein was not yet present. The col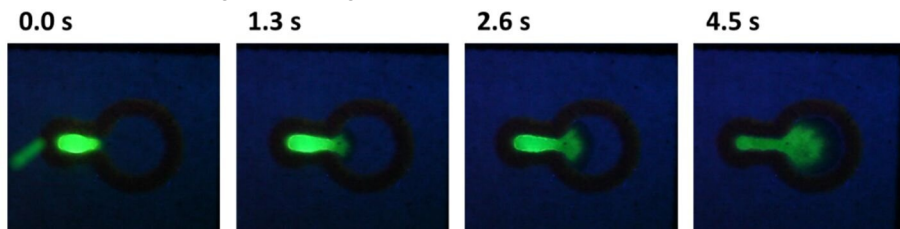or intensity variation was extracted for a number of specific geometric points along the channel. These data were then calibrated with the concentration of the solution by assigning the maximum value obtained for the colour intensity to the initial concentration value. Finally, the approximate concentration value at each chosen distance along the channel surface was plotted as a function of time, **Figure 5.14 B)**.

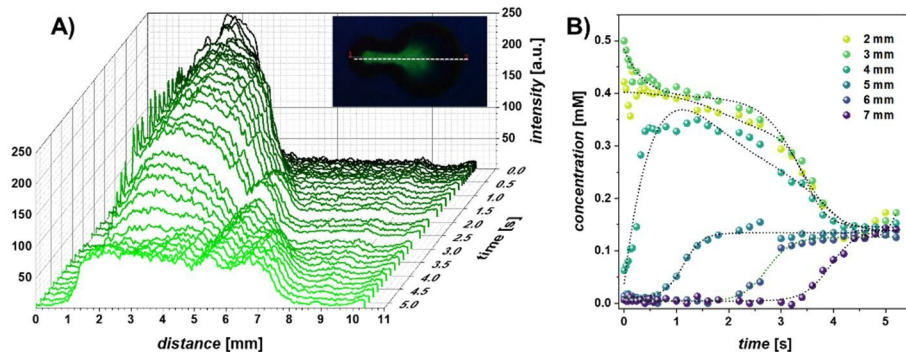**Figure 5.14. A)** Colour intensity profile along the channel and over time. **B)** Approximation of the concentration distribution evolution at different points along the channel. Inset: The midline along which the colour intensity profile was extracted.

At the initial time (t = 0), the concentration is maximum at 2 and 3 mm distance from the channel inlet, and has a value of 0 at the end of the channel. During diffusion, the concentration decreases at the inlet region and increases towards the end of the reservoir, finally reaching the same value, approximated as 0.1 mM, along the entire length of the channel. The calculated value is 5 times lower than the initially injected value, showing a significant reduction of the. However, reaching the same value in the end is a result consistent with the theory that under the action of the concentration gradient, systems tend towards equilibrium.

Droplet interface evolution during diffusion

In order to analyse the evolution of the interface, the experiments involved viscoelastic solutions, as their diffusion will be slow and interface identification can be carried out with a greater accuracy. Thus, fluids with different concentrations of PEO were included in the study, in order to have a broad understanding of the phenomenon. By using viscoelastic solutions of PEO, the applicability of the studies can be extended, as these can be models for fluids resulting from industrial activities or of biological interest. In addition, PEO is a water-soluble polymer, eliminating the necessity for strong solvents, whose rheological properties could influence the diffusion process.

The evolution of the fluid interface was analyzed for both low and high viscosity fluids, with polymer concentrations ranging between (0.05 - 2.5) % (w/v). Using the numerical procedure described in **Chapter 4**, the time evolution of droplet diameter and diffusion velocity, as well as contact angle and volume could be extracted from the interface numerical representation, **Figures 5.15 - 5.16**.

For all the fluids used, an inflection point in the diameter evolution could be identified and it was attributed to the transition between the two diffusion phases. When the fluid came into contact with the porous medium, it started to rapidly diffuse on the surface of the substrate until it reached a critical diameter. (the spreading phase) Subsequently, the droplet began to shrink under the action of the capillary force as it was absorbed into the substrate (the absorption phase).
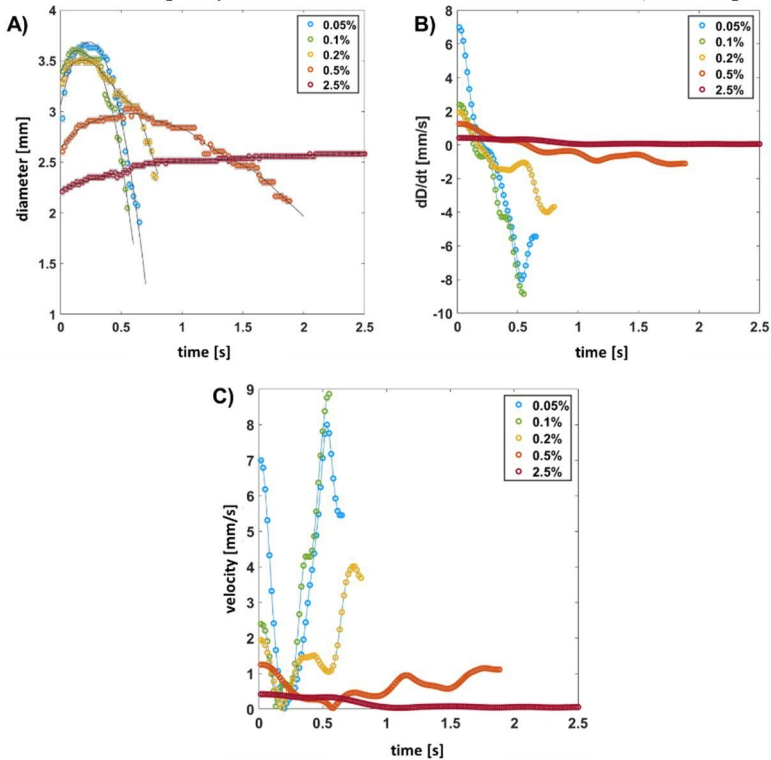
Figure 5.15. Evolution over time of **A)** diameter, **B)** first order derivative and **C)** diffusion velocity for PEO droplets with different concentrations.

For low viscosity fluids, both phases could be observed, the transition between the two being indicated by the point at which the derivative reaches zero. By plotting the absolute value of the derivative, it can be seen that the two diffusion phases occur at similar rates, the predominant influence being given by the material characteristics of the fluid used. In the case of the 2.5% PEO solution, after reaching a critical value of the diameter, the flow enters a slow transient regime, being hardly absorbed into the substrate due to high viscosity.

Fitting the data points with a smooth function allowed a representation of the diameter evolution with high accuracy, taking into account the discontinuity areas. The local maxima and minima observed in the evolution of the derivative were attributed to the inhomogeneity of the porous medium, the fluid diffusion being influenced by the spatial distribution of the pores, as well as their size.

Figure 5.16. Variations of **A)** contact angle and **B)** drop volume.

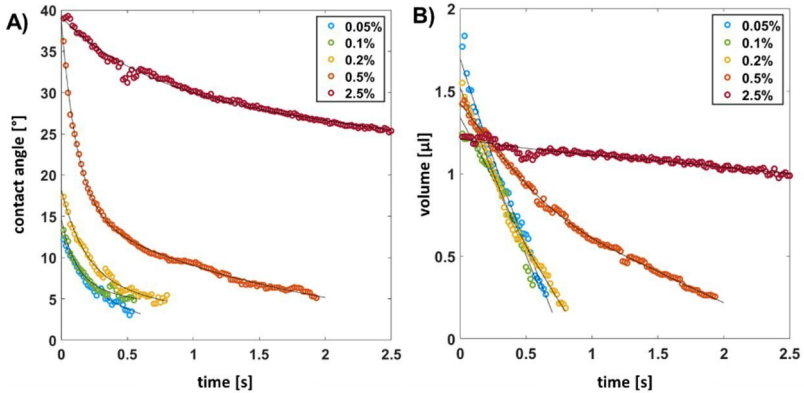In the case of contact angle and volume evolutions, no areas of high discontinuity were identified and the experimental data fitting was performed using exponential functions. Since the volume evolution shows a decrease from the early stage of the absorption phenomenon, it can be concluded that diffusion through the substrate occurs from the first identified stage, and it is not a redistribution of the fluid volume on the substrate surface.

The initial velocities reached by each fluid were plotted as a function of solution concentration and viscosity, **Figure 5.17**. A dependence between the maximum advancing velocity of the fluid front in the expansion stage and the solution concentration was observed, **Figure 5.18 A)**, which can be described by the equation $v_{max}(C) = a \, C^b$, where $a = -0.14$ and $b = -0.65$.
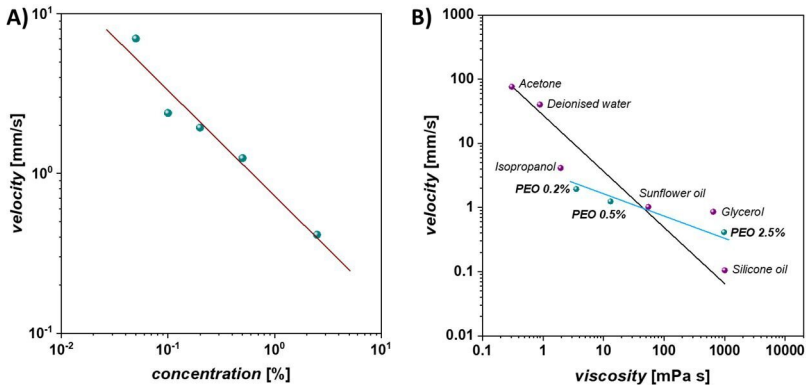
Figure 5.17. Diffusion velocity as a function of **A)** concentration and **B)** viscosity.

Considering the viscosity values for three of the investigated PEO solutions, the velocity values have been plotted together with the previously obtained results, **Figure 5.17 B)**. Since the concentration of a polymer solution directly influences its viscosity, the two dependencies are similar. However, PEO solutions also have an elasticity component, which may have an influence on the diffusion velocity, and differences from the behaviour of Newtonian fluids are observed. In the case of PEO solutions, the velocity dependence on the viscosity was fitted with the equation $v_{max\,PEO}(\eta) = a \, \eta^b$, where the values identified for a and b were 0.24 and -0.20, respectively.

Chapter 6. Fabrication and characterization of porous surfaces

Porous micro- or nano-structured materials have a high potential for application, being on the same scale as particulate matter (PM) and macromolecules, and can be thus used to filter, capture or immobilise nanoparticles and chemical compunds. In this chapter, electrospun and rotary-jet spun polymer fiber meshes made of cellulose acetate (CA) and poly(methyl methacrylate) (PMMA) were fabricated. The first objective of the study was to investigate the influence of relative humidity on the process and the morphology of the resulting fibers. This parameter was chosen because of its high influence on the process, directly affecting the solvent evaporation time and subsequently the uniformity of the fiber structure and the homogeneity of the meshes. The second objective was to evaluate the electrical and electrochemical properties of metallized polymer meshes, the final goal being the fabrication of electrodes with fibrillar structure.

Rheological properties

The study included CA solutions of different concentrations and solvent mixtures, **Table 6.1**. The rheological study was carried out for the solutions *S3*, *S5* and *S6*, and the variation of viscosity over time was evaluated. Attention was focused on the solution viscosity, being considered the property of major influence over the process, **Figure 6.1**. The viscosity value assigned to each solution was considered the value obtained at t = 0. From the linear section of the viscosity evolution over time, a viscosity increase coefficient was evaluated as the slope of the fitting curve, the obtained values being shown in **Table 6.1**.

Table 6.1. CA solutions used and the values determined for initial viscosity and the viscosity increase coefficient.

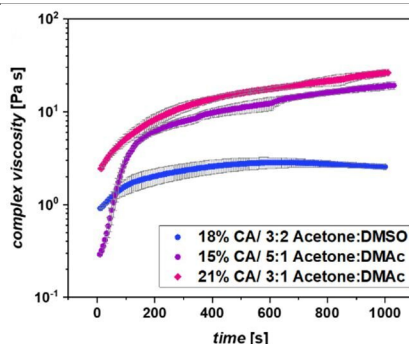| Solution	Solvent	Ratio (v/v)	CA (%)	Viscosity at 22.5 °C (Pa s)	Viscosity increase coefficient (Pa)
S1	Acetone/water	20/1	17		
S2		10/1	21		
S3	Acetone/DMAc	5/1	15	0.3 ± 0.01	0,011
S4		5/1	21		
S5		3/1	21	2.5 ± 0.10	0,004
S6	Acetone/DMSO	3/2	18	0.9 ± 0.02	0,003

Figure 6.1 Time evolution of viscosity (η^*), evaluated at the temperature 22.5 °C and angular velocity 10 rad/s.

It was observed that the viscosity evolution over time for solutions formed with the same solvent mixture (*S3* and *S5*) presents a similar trend, the main difference being the initial viscosity value, which is directly influenced by the polymer concentration. The rapid increase in viscosity of *S3* was attributed to the higher concentration of acetone, being a compound with higher volatility than DMAc. The acetone:DMSO solvent mixture was considered the most stable, since upon prolonged exposure to the atmosphere, the viscosity value does not change substantially. The initial viscosity value was considered as a reference parameter, since in electrospinning and rotary-jet spinning techniques, droplets are exposed for short periods (on the order of seconds) to air before they turn into filaments.

The influence of humidity on the electrospun fiber mesh morphology

a. Cellulose acetate

The electrospinning process was tested for relative humidities ranging from (25 - 75)%. For all the solutions studied, regardless of the solvent or polymer concentration used, the optimal results were obtained at high humidity values, which consisted of increased fibre density and a high degree of fiber uniformity. The diameters of the resulting fibers in relation to the solutions and humidity values, are shown in **Figure 6.2**.
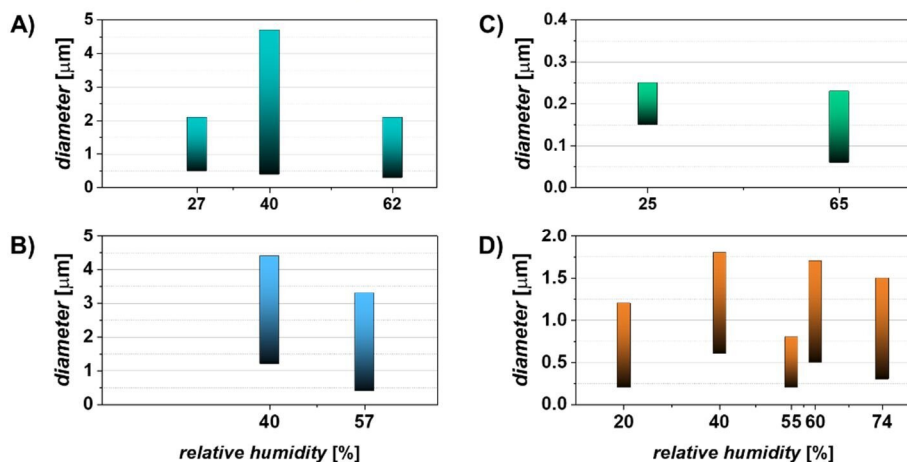
Figure 6.2. Diameter of electrospun fibers resulted at different relative humidity values for **A)** *S1*, **B)** *S2*, **C)** *S3* and **D)** *S4*.

Different fiber morphologies were identified depending on the solvent used and the relative humidity in the enclosure, **Figure 6.3**. The meshes fabricated from acetone:water solutions (*S1* and *S2*) have a ribbon shape, unlike those from acetone:DMAc (*S3* and *S4*), which have a regular cylindrical shape. In the case of solution *S3*, elliptical polymer agglomerations due to low humidity were identified, a morphology defined in the literature as "beads on fibers". The influence of viscosity could be observed by analyzing the fibers produced from solutions *S3* and *S4*. In the case of *S4*, which has a higher viscosity due to the higher polymer concentration, the fibers were uniformly elongated in the electric field, having a smooth surface. In the case of *S3*, regardless of the relative humidity within the enclosure, the meshes presented defects.

Figure 6.3. Fibers fabricated from different solutions resulting in different morphologies: **A)** ribbons (*S2*), **B)** "beaded fibres" (*S3*), **C)** cylindrical fibres (*S4*).

b. Poly(methyl methacrylate)

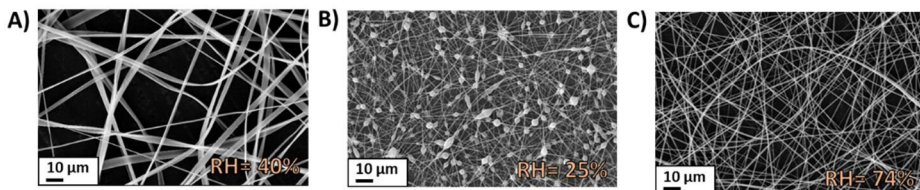In the case of electrospun PMMA fibres, the influence of environmental parameters on the process efficiency was evaluated. Different samples were obtained, for which the process efficiency was quantified by the fiber density obtained, while the electrospinning time was kept the same for all samples. The fiber density was quantified by analysing the optical transmittance of the resulting meshes.

It was experimentally observed that in the case of PMMA solutions, the temperature and humidity value ranges in which the meshes could be fabricated were much narrower. An increase of 8% in relative humidity led to a drastic decrease in mesh fabrication and collection efficiency, **Figure 6.4 C)**. Optimal temperature and relative humidity conditions were found to be 21-22 ºC, respectively 20-25%, which determined a high process efficiency and fibers with uniform, defect-free structure **Figure 6.4 A), B)**.
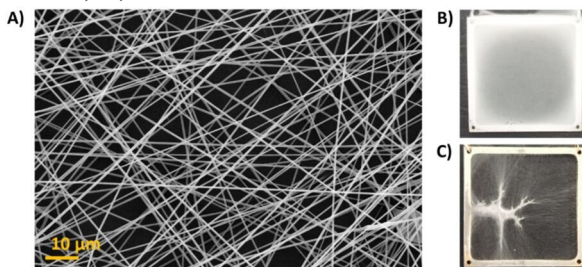
Figure 6.4. **A)** Morphology of electrospun PMMA fibres under optimal temperature and relative humidity conditions (22 ºC, 25% respectively) analysed by scanning electron microscopy. Photographic mages of PMMA meshes fabricated at 22 ºC, under relative humidity conditions of **B)** 30% and **C)** 38%.

Porosity evaluation

The CA solutions were subjected to continuous electrospinning in order to produce functional porous layers of high density, for applications requiring absorbent materials. The thickness and surface porosity of the deposited layers were approximated from electron microscopy images and compared with the characteristics of the filter paper, **Figure 6.5**. The surface porosity was determined as the ratio of the total black area (pores) to the total area of the analysed image in binary format, **Figure 6.5 A2)-B2)**.

Similar to the previous results, the solvent volatility had a high influence on the process. The high acetone concentration of *S4* resulted in a low collection yield, with the deposited layer having a thickness of 45 µm after 30 minutes of collection. In the case of *S5*, the layer deposited after 30 minutes reached a thickness of 155 µm, a value close to the thickness of filter paper (200 µm). It was thus concluded that high fiber densities could be achieved by electrospinning and the

thickness of the deposited layer could be similar to filter paper. However, the diameter of the electrospun fibres was much smaller than the one of cellulose fibres in paper, and the porosity much higher. Therefore, for the case of a fluid in contact with these polymer porous substrates the behavior would be different than for the case of filter paper.
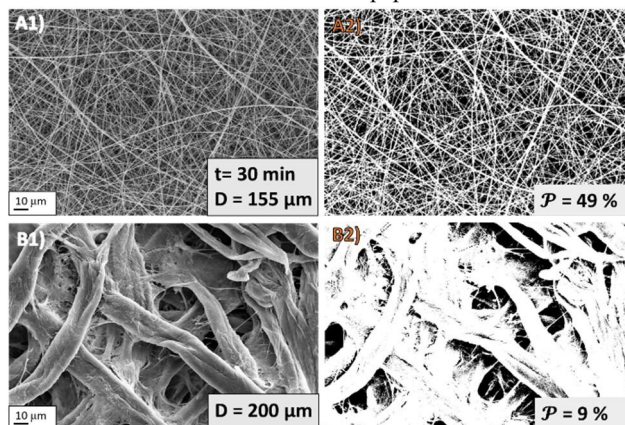
Figure 6.5 Morphological comparison of **A1)** electrospun mesh from *S5* solution and **B1)** filter paper. **A2)-B2)** Representation in binary format of electron microscopy images and the numerically evaluated surface porosities.

Wetting properties assessment

On the surface of the PMMA meshes, 20 µl droplets of a 500 µM MB solution were deposited. Both the unmodified PMMA meshes, **Figure 6.6 A)**, and thermally attached meshes on polyethylene terephthalate (PET) films, **Figure 6.6 C)**, were investigated. The PMMA meshes were chosen for this study due to their superior mechanical strength.
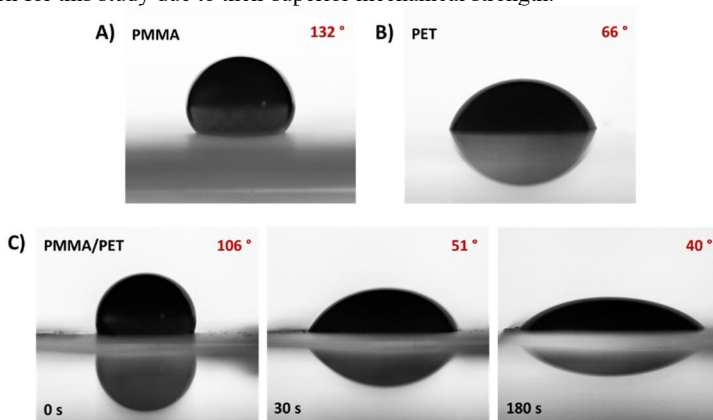
Figure 6.6 Contact angles measured for 20 µl 500 µM MB droplets deposited on **A)** unmodified PMMA mesh, **B)** PET film, **C)** PMMA/PET assembly shown at different time periods.

A strong hydrophobic character of the fabricated meshes was observed, but their integration with a hydrophilic substrate resulted in a transient behaviour. For the time interval investigated (3

min), no considerable changes of the droplet interfaces placed on PMMA or PET were observed. However, in the case of the PMMA/PET assembly, rapid changes of the interface were observed, as it diffused on the substrate surface. This behaviour could also be attributed to a laminar flow at the interface between the two substrates, as no chemical mediator (adhesive) was present between them. It was thus concluded that the integration of the meshes with a substrate with hydrophilic properties would cause the whole assembly to tend towards hydrophilicity.

The influence of rotation speed on the morphology of rotary-jet spun meshes

The volatility of the solvents used also had a pronounced effect on the rotary-jet spinning process. Thus, from the solutions *S1* to *S4* fibers could not be produced, as the polymer dried at the needle tip before they could be elongated by the centrifugal force. Polymer meshes could be fabricated from solutions *S5* and *S6*, and the results obtained under the influence of the rotation speed are centralised in **Figure 6.7**.
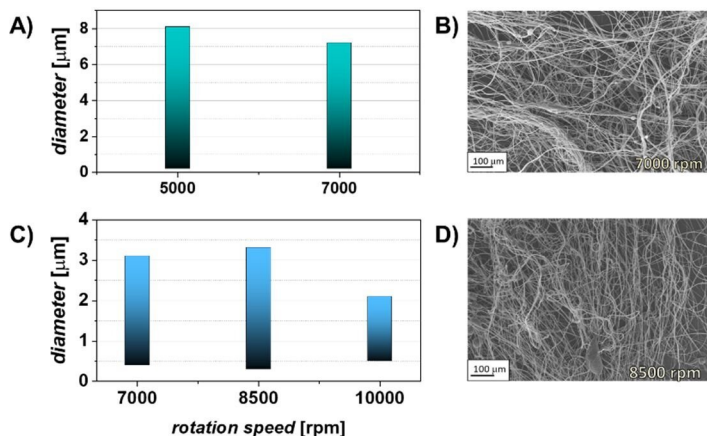
Figure 6.7. Diameters and morphologies of the fibers obtained by rotary-jet spinning for solutions **A), B)** *S5* and **C), D)** *S6*.

Rotary-jet spun meshes were produced with high densities, but the degree of uniformity was considerably lower than for the electrospun meshes, and the overall structure of the deposited material was inhomogeneous and non-isotropic. For the *S5* solution, defects characterized by spherical polymer agglomerations occurred at any rotation speed value, an optimal value was thus not found. In the case of solution *S6*, a wider range of values in which the meshes could be produced was found, with higher fiber uniformity, a degree of ordering being also observed. The optimal rotation speed value was considered 8500 rpm, as the occurrence of defects along the fibers was minimal.

The differences in the results between the two solutions can be explained by considering the viscosity previously obtained (2.4 Pa s for *S5* and 0.9 Pa s for *S6*). A solution of lower viscosity will act with a lower force opposed to the centrifugal force, being able to be uniformly elongated, while polymer agglomerates have a lower probability to form.
mai uniform alungită, iar aglomerările de polimer având o tendință mai mică să se formeze.

Electrical and electrochemical characteristics

For the analysis of the electrical and electrochemical characteristics, electrospun PMMA meshes of different densities were fabricated and the optical transmittance of the resulting meshes

was evaluated spectrophotometrically in the visible range. The reference value for the comparison between the meshes was chosen to be the 550 nm spectral band. Afterwards, a 100 nm gold layer was deposited on the surface of the meshes, which were subsequently thermally transferred onto PET foils, resulting in a Au/PMMA/PET assembly. The flexible electrodes thus formed were subjected to resistivity measurements in two and four points, **Figure 6.8**, as well as electrochemical measurements in a three-electrode configuration in the presence of $K_4[Fe(CN)_6]$, **Figure 6.9**, using a Ag/AgCl reference electrode and a Pt auxiliary electrode. Evaluation of the characteristics of the meshes was carried out by analysing the current density variation, recorded at a scan rate of 25 mV s^{-1}.
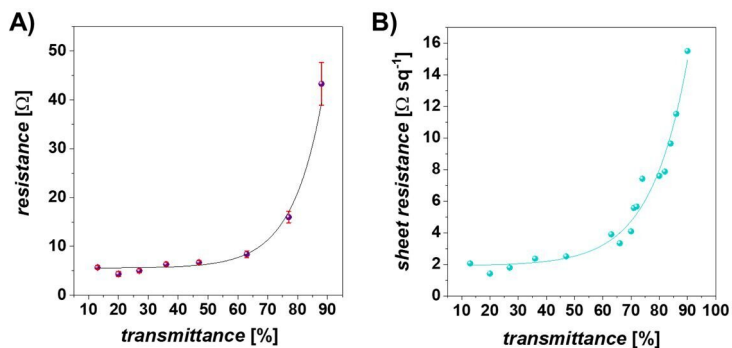
Figure 6.8. Variation of electrical resistance measured in **A)** two and **B)** four points as a function of fiber mesh optical transmittance.
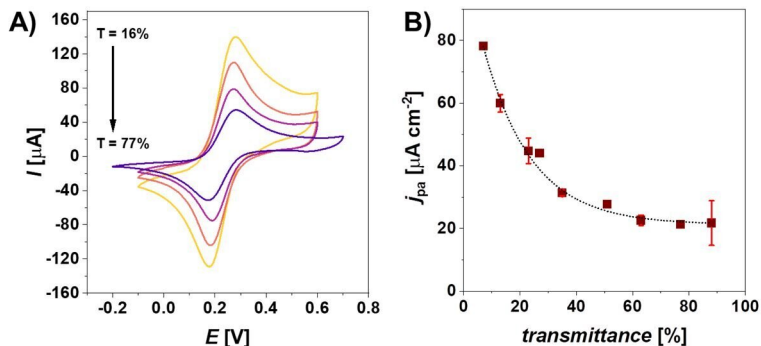
Figure 6.9. A) Cyclic voltammograms recorded with Au/PMMA/PET electrodes, performed in the presence of 5 mM $K_4[Fe(CN)_6]$, in phosphate buffer (pH 7), at a scan rate of 25 mV s^{-1}. **B)** Variation of anodic peak current as a function of mesh transmittance.

Electrical measurements showed a minimum variation in resistance for meshes with optical transmittance in the range (10-50) %, followed by an exponential increase. In the case of the electrochemical measurements, the effect was more pronounced, observing a 50% reduction in current density for a 20% change in transmittance. It was thus concluded that the electrospun fiber meshes viable to become flexible electrodes were those whose transmittance values fall between (10-20) %, in which case the electrical charge transfer at the electrode-fluid interface had a high efficiency.

Chapter 7. Applications

Portable electrochemical devices designed for sensor applications have the advantage of being able to be integrated with electronic circuits for measurements and data transmission, and the power supply of these integrated systems can be provided by low voltage batteries (1.5 V) [9]. In this way, systems for continuous monitoring of water quality, atmosphere or health status can be developed with low power consumption. Industrial or environmental applications include the detection of heavy metal ions (Cd(II), Pb(II) [45]), pesticides (organophosphates [46], carbamates [47]) or toxic compounds (phenols [48]). For biological applications, ions, small molecules, proteins and nucleic acids in body fluids can be detected by electrochemical techniques [49].

In this chapter, procedures for fabricating a portable electrochemical cell based on porous-structured materials with a paper substrate and fibrillar electrodes made of electrospun PMMA meshes were implemented. The study focused on identifying the optimal configuration of the electrochemical cell in terms of stability and reproducibility. Finally, the electrochemical cell was evaluated for the detection of hydrogen peroxide, a chemical compound of industrial and biological interest, glucose and nucleic acids, molecules that can be used for continuous monitoring of chronic or pandemic diseases.

7.1 Fabrication and characterisation of electrochemical devices with porous substrates

Conductive layers of Au, Ag, Pt and Pd were deposited on the surface of the polymer meshes, which will represent the contact interface between the electrodes and the fluid diffusing through the porous medium. The morphology of the deposited layers was investigated by scanning electron microscopy, **Figure 7.1 A1)-D1)**. In order to characterise the surface of the deposited layers, an image processing algorithm was developed, thus achieving the identification of single crystals and quantifying their surface area, **Figure 7.1 A2)-D2)**. The influence of the deposited metal layers on the wetting properties of the meshes was investigated by contact angle measurements, performed accordingly to the procedure described in the previous chapter.

In the case of the Au and Ag layers, a reduction of the previously measured contact angle (132°) was observed. Similarities were observed between the two metals both in terms of layer morphology and contact angle value. Similarities could also be seen in the case of Pt and Pd, for which the hydrophobic character was slightly accentuated. In the case of platinum, the fibres were covered with a low grain size main layer, on top of which single crystals were formed. The palladium deposition resulted in the formation of a low grain size layer with a large distribution of particles with areas of about 100 nm. Correlating these results, it can be considered that the granulation of the deposited metal layer will cause different behaviours at the contact interface with a fluid, influencing the wall slip phenomena.

The fabrication of the electrochemical cell involved integrating the metallised polymer meshes with paper. The procedure was achieved by heat treatment of the two surfaces brought into contact. Electron microscopy investigations showed that the structure of the meshes remained intact after the thermal transfer onto paper, no discontinuities of the fibers or the metallic layer being observed, thus concluding that the transfer procedure does not affect their conductivity, **Figure 7.2**. Moreover, the porous structure of the paper was unaffected by the meshes deposited onto its surface, thus considering that the fluid diffusion through the porous substrate will not be influenced by the electrodes formed on its surface.
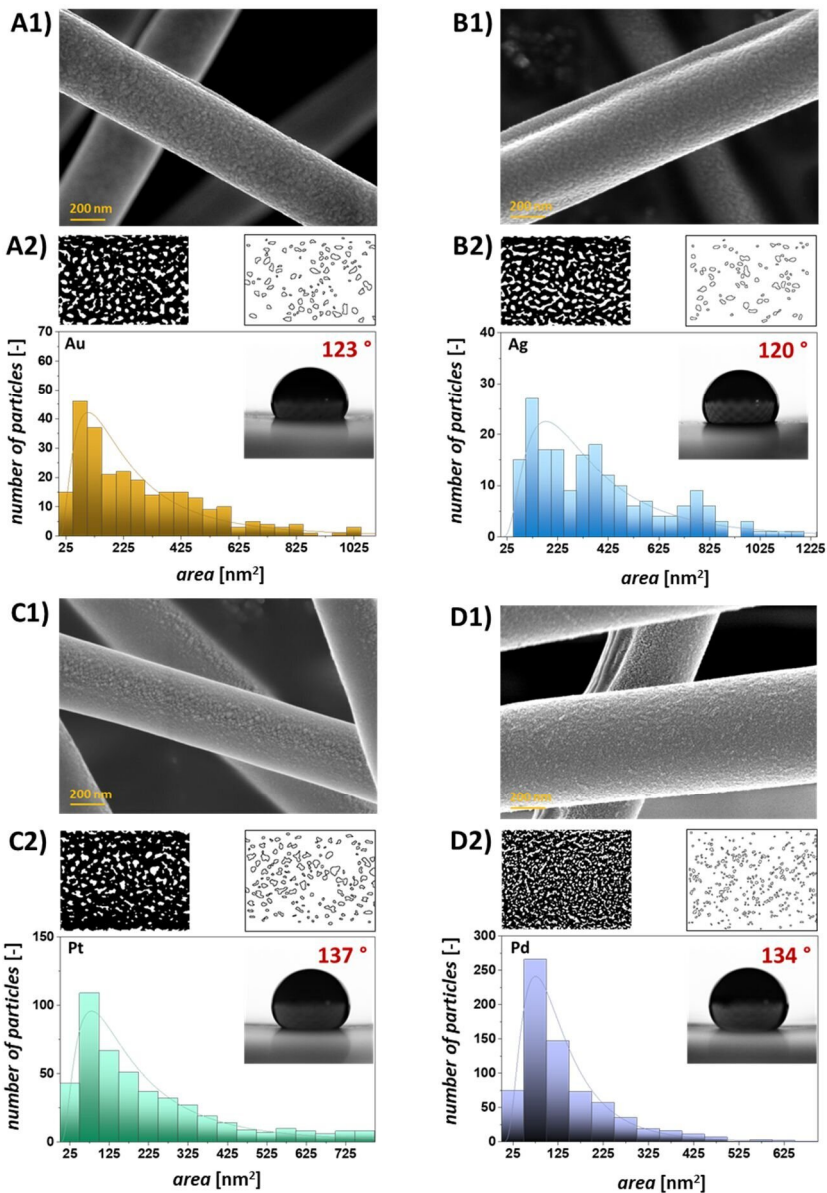
Figure 7.1 Scanning electron microscopy images of PMMA fibers metallised with **A1)** gold, **B1)** silver, **C1)** platinum, **D1)** palladium. **A2)-D2)** Representation of the images in binary format, along with the identified crystals and their area distribution. Insets: views of the contact angle between 20 µl 500 µM MB droplets and the metallized PMMA meshes.
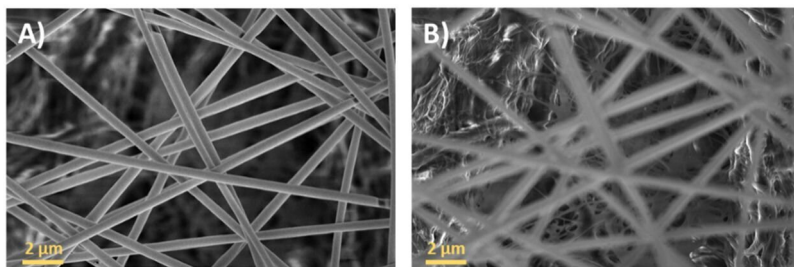
Figure 7.2 Ansamblul hârtie-plase polimerice cu focalizare pe **A)** plasele polimerice, **B)** hârtia cromatografică.

In order to obtain an optimal configuration for an electrochemical sensor, but also to understand the behavior of electroactive species at the electrode-paper interface, multiple architectures with incremental complexity were developed. Four electrochemical cell configurations were fabricated, designed in two- or three-electrode architectures, **Figure 7.3**. Of these, one involved fabricating the device without a fluidic channel, and three were designed with a 3D printed fluidic channel. Their electrochemical characterization was performed in the presence of redox probes, $K_4[Fe(CN)_6]$ and MB. In order to fabricate multiple electrodes from a single polymeric mesh, 3D printed masks were fabricated, with which selective metallisation could be achieved. Finally, 3D printed supports with Pt or Cu plates were fabricated for ensuring the connection to the potentiostat.

The *Configuration IV* was considered optimal, as the influence of the non-Faradaic currents was low, and a clear definition of the anodic and cathodic current peaks was observed, which are specific to charge transfer reactions, by oxidation and reduction of the investigated chemical species. The electrodes were fabricated with corner-free boundaries, as these could lead to the local high current densities and thus to non-uniformities in the charge distribution at the electrode surface. The working and reference electrodes were placed on the upper side of the paper, and the auxiliary electrode on the lower side. The *Configuration IV* was studied by fabricating all three electrodes from Au, as well as using Ag for the reference or Pt and Pd for the working electrode.

The behaviour of the electrochemical cell fabricated in *Configuration IV* was subsequently investigated by cyclic voltammetry in $0.1M$ H_2SO_4 in order to determine the potential limits, the minimum volume needed and the influence of scan rates on the current, **Figure 7.4**. Characterisation was carried out in the potential range $[-0.75; +1.40]$ V (*vs*. Au), where four distinct processes were identified. The anodic component of the voltammogram showed the specific peak of oxide/hydroxide formation at the electrode surface at potentials higher than $+0.75$ V being limited by the water hydrolysis reaction at potentials higher than $+1.25$ V. The cathode component shows the peak corresponding to the reduction of oxides/hydroxides in the range $[+0.6; +0.25]$ V and the hydrogen evolution reaction for potentials below -0.50 V. The optimal potential range was determined to be $[-0.40; +1.40]$ V.

It was observed that the current intensity increased with volume up to 25 µl and remained constant thereafter, this value being thus considered to be the minimum necessary for the correct operation of the device. However, in order to counterbalance the effect of evaporation, the optimum measurement volume was considered to be 40 µl. Varying the scan rates, does not bring drastic changes on the electrochemical behaviour, oxidation and reduction processes being clearly defined and the influence of the non-Faradaic currents minimal.
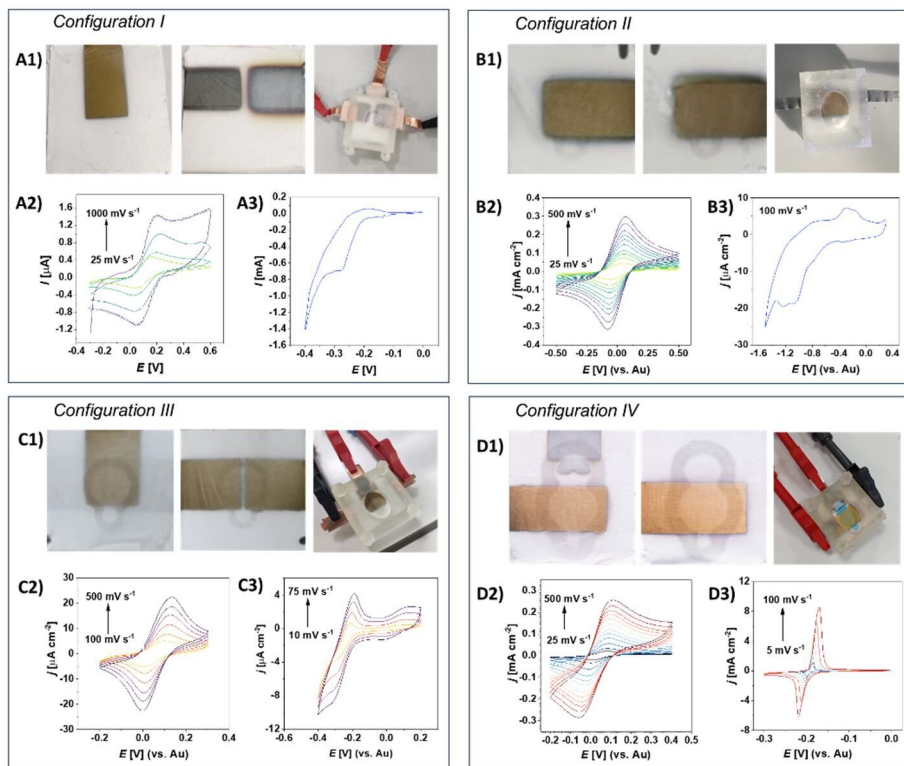
Figure 7.3. Electrochemical cell architectures consisting of electrodes arranged on each side of the paper, **A1)** without fluidic channel and **B1) - D1)** with 3D printed channel. Electrochemical characterisations performed by cyclic voltammetry in phosphate buffer (pH 7.2) in the presence of **A2), B2), C2), D2)** 2 mM $(Fe(CN)_6)^{3-/4-}$ and **A3), B3) C3), D3)** 10 mM MB.
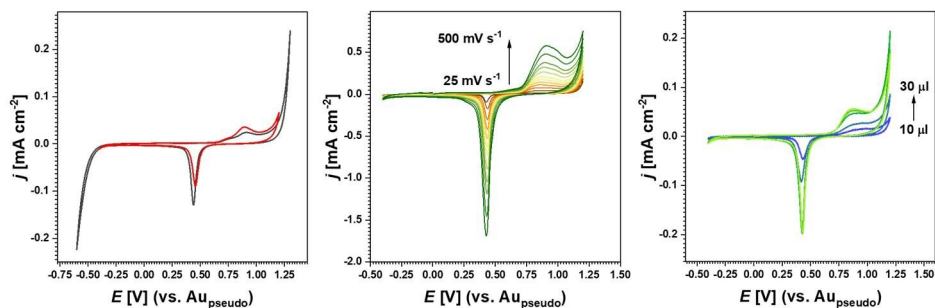
Figure 7.4. Cyclic voltammograms performed in 0.1 M H_2SO_4 for evaluating **A)** potential limits, **B)** influence of scan rate on the current, **C)** optimal solution volume.

In the case of using platinum or palladium for the working electrode, it was necessary to place the device in controlled nitrogen flow, in the absence of which the peaks specific to the

38

redox reactions could not be identified, **Figure 7.5**. As the deposited layer has a low grain size for the two metals and the layers have a strong hydrophobic character, a possible cause of this behaviour was considered to be the adsorption of molecular oxygen from the ambient atmosphere on the electrode surface, influencing the fluid wall slip for the electrode-liquid interface. Since in the case of gold this phenomenon was not observed, and the device was designed with the aim of being functional outside a controlled environment, it was concluded that the use of gold for the working electrode determines the desired degree of stability.
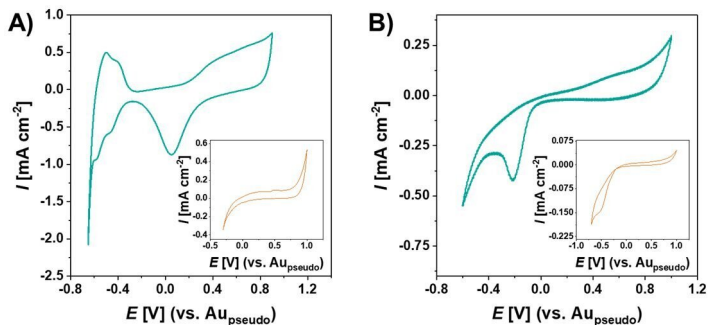
**Figure 7.5** Cyclic voltammograms carried out in acidic medium for electrochemical cell fabricated with working electrode made of polymeric meshes metallized with **A)** Pt (in H_2SO_4 pH 1.0) and **B)** Pd (in acetate buffer pH 4.5), at a scan rate of 100 mV s^{-1}, under constant flow of N_2. Insets: Voltammograms performed in ambient atmosphere without N_2 flow.

Finally, the device was characterized by electrochemical impedance spectroscopy in phosphate buffer to determine the equivalent circuit and the stability of the system over time. The stability of the system was analysed in open circuit for four frequency values (1; 10; 100; 1000) Hz, **Figure 7.6**.
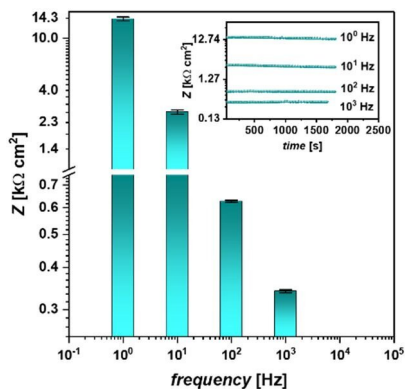
Figure 7.6. Time evolution of the impedance evaluated in open circuit for four frequency values, (1; 10; 100; 1000) Hz.

It was observed that the impedance value remained constant for measurements recorded for 1600 s. This demonstrates the possibility of performing impedimetric detections and the certainty that any change in impedance is a result of the interaction with analytes injected into the electrochemical cell.

7.2 Sensor for detection and quantification of analytes present in sweat

In this sub-chapter, a biosensor with paper substrate and electrospun fiber mesh electrodes was developed according to *Configuration IV* for monitoring analytes in body fluids, as a method to provide a profile of the parameters related to the physiological state of an organism in real time [50]. The concentrations of molecules such as glucose, lactic acid or uric acid in biological fluids (blood, sweat, urine, tears) are directly related to the processes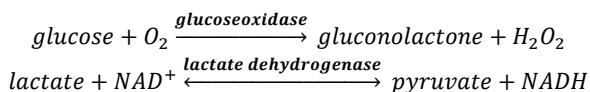 taking place in the human body, and their values can provide information about the health status of an individual [51]. The general approach in biosensor development involves using enzymes specific to the molecules of interest and detecting the reaction by-products, such as H_2O_2 in the case of oxidases, or co-enzymes, such as nicotinamide adenine dinucleotide (NADH/NAD$^+$) in the case of dehydrogenases, according to the reactions:

$$glucose + O_2 \xrightarrow{glucoseoxidase} gluconolactone + H_2O_2$$

$$lactate + NAD^+ \xleftarrow{lactate\ dehydrogenase} pyruvate + NADH$$

In a first step, the functionality of the sensor was analysed for the amperometric detection and quantification of hydrogen peroxide (H_2O_2) and nicotinamide adenine dinucleotide (NADH). Measurements were performed at both positive and negative potentials, **Figure 7.7**, in neutral and acid media. The current variation is represented by a positive or negative step depending on the applied potential, which induces oxidation and reduction reactions of H_2O_2, respectively. The sensor calibration curves, i.e. the correlation between current variation and analyte concentration, were shown to be linear functions described by the equation $\Delta j = a + b \cdot [analyte]$. The sensitivity of the sensor was determined as the slope (b) of the fitting line. The limit of detection (LOD) was evaluated as $LOD = 3\ SD/b$, where SD is the standard deviation of the slope. The limit of quantification (LOQ) was determined as $LOQ = 10\ SD/b$. The sensitivities, detection limits and linearity ranges obtained for each measurement are presented in **Table 7.1**.
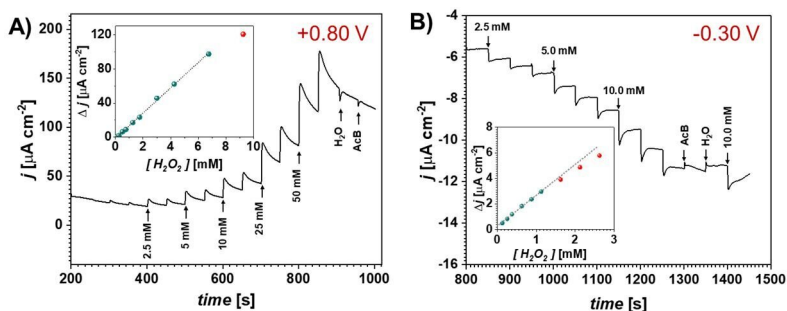
Figure 7.7. Amperometric measurements recorded with successive additions of H_2O_2 in acetate buffer (pH 4.3) at **A)** positive and **B)** negative potentiala. Insets: the calibration curves.

Subsequently, portable sensors were developed and tested for glucose detection in both electrolyte buffer solutions and artificial sweat, **Figure 7.8**. For this purpose, prior to the measurements, the enzyme glucoseoxidase (GOx) was immobilized in the microfluidic channel. The working potential for the amperometric measurements was chosen according to the results obtained by cyclic voltammetry, **Figure 7.8 A)**. Thus, glucose detection was performed in the potential range where an increase in current was identified in the presence of GOx and glucose, but outside the region where other reactions (such as oxide formation) are present.

Table 7.1. Sensitivity, detection limit and linearity range calculated for H_2O_2 and NADH detection.

Analyte	pH	E_{app} (V)	Sensitivity ($\mu A\ cm^{-2}\ mM^{-1}$)	LOD (μM)	Linearity range
H_2O_2	4.3	+ 0.8	14.8	270	below 6.75 mM
		- 0.3	2.5	59	below 1.2 mM
	7.2	+ 0.5	0.1	821	< 40 mM >
		- 0.5	6.9	1220	below 21 mM
NADH	7.2	+ 0.8	12.8	83	below 1.25 mM
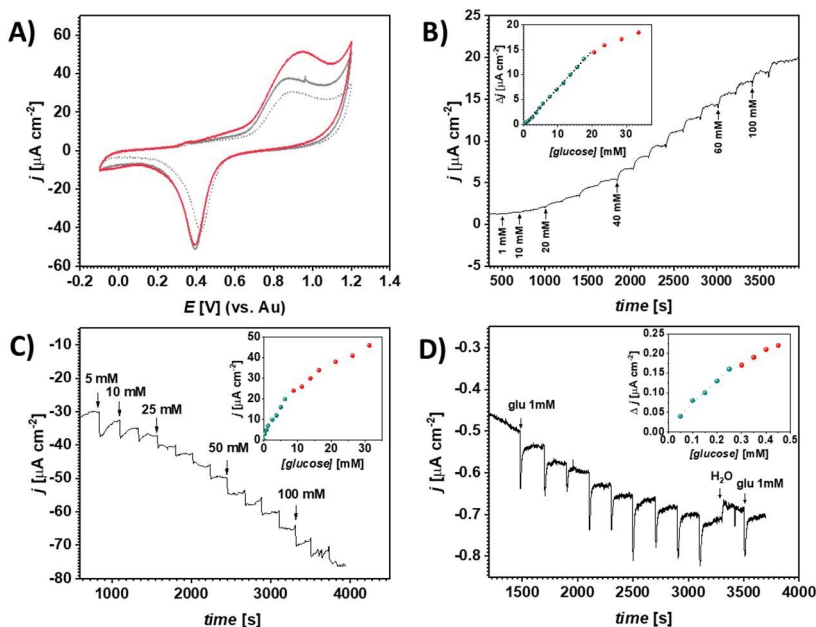
Figure 7.8. **A)** Cyclic voltammogram performed in phosphate buffer in the absence (dashed curve) and in the presence of glucose (black curve) and GOx (red curve). Amperometric measurements with glucose additions in **B)** phosphate buffer, E_{app} = +0.4 V (*vs.* Au), **C)** acetate buffer, E_{app} = -0.4 V (*vs.* Au), **D)** artificial sweat (pH 5.8), E_{app} = -0.2 V (*vs.* Ag). Insets: calibration curves.

Glucose detection was initially investigated in phosphate buffer pH 7.0, at an applied potential E_{app} = +0.40 V, the biosensor response being in the form of positive current steps due to H_2O_2 oxidation reactions, **Figure 7.8 B)**. Under these conditions a detection limit of 0.73 mM was observed, **Table 7.2**, a value relevant for glucose measurements in biological media. However, it is preferable that glucose detection is performed at negative potential values to avoid interferences from other compounds, such as uric acid or dopamine, which may undergo oxidation reactions at potential values similar to those for H_2O_2 detection. Thus, glucose detection was investigated in acetate buffer at an applied potential E_{app} = -0.40 V, the biosensor response being in the form of negative current steps due to reduction reactions of H_2O_2, **Figure 7.8 C)**. Under these conditions a detection limit of 1.00 mM was observed.

Table 7.2. Sensitivity, detection limit and linearity range calculated for glucose detection.

Electrolyte	E_{app} (V)	Sensibility ($\mu A \ cm^{-2} \ mM^{-1}$)	LOD (μM)	Linearity range
Phosphate buffer (pH 7)	+ 0.4	0.74	730	below 17 mM
Acetate buffer (pH 4.3)	- 0.4	2.85	1000	below 6.25 mM
Artificial sweat (pH 5.8)	- 0.2	0.58	25	below 0.25 mM

Similar measurements were also performed in artificial sweat, **Figure 7.8 D)**, to simulate biosensor functionality in environments as close as possible to the real ones. In this case, the detection limit recorded was below the normal values of glucose in human sweat (0.06-0.2 mM), **Table 7.2**, demonstrating the applicability of the sensor for continuous monitoring systems in sweat.

7.3 Senzor pentru detecția și cuantificarea acizilor nucleici

For the detection of nucleic acids, the sensor was fabricated in *Configuration IV* and two strategies were addressed. The first strategy involved voltammetric detection in the presence of MB, as it has the property of interacting with nucleic acids both under the action of electrostatic forces and by intercalation between nitrogenous base pairs. The second detection strategy involved impedimetric measurements in the absence of any marker. Due to the dielectric nature of nucleic acids, their presence in an electrochemical system will cause changes in capacitance, which can be investigated by electrochemical impedance spectroscopy, analysing the variation of the imaginary component of impedance.

Since voltammetric detection depends on the interaction of nucleic acids with MB, in a first step the molecular interaction in the porous substrate was studied by optical and spectroscopic investigations. Visualizations of the interaction of the two compounds on chromatographic paper, **Figure 7.9 A)**, showed on the one hand a uniform distribution of MB in the analysis zone, even after successive additions of solvent (H_2O), and on the other hand changes in colour intensity after successive additions of double-stranded nucleic acids (dsDNA). These changes are dependent on both the concentration of nucleic acids and the interaction time. The results obtained on the paper substrate were compared with those obtained on a glass slide, **Figure 7.9 B)**, substrate used as control. It was observed that the phenomenon occurs similarly on both substrates, thus demonstrating that the molecular interactions could take place within the porous matrix, with no influence of the paper substrate on the reaction. Optical microscopy analysis of the glass slide dried samples, **Figure 7.10**, showed the presence of fibrillar structures, whose density is directly proportional to the concentration of added nucleic acids. These fibrillar structures were not identified in the case of the pure unmodified MB sample, indicating that their formation is a result of MB aggregation on the nucleic acid chain.

Raman spectroscopy measurements, **Figure 7.11 B)**, were performed on the chromatographic paper before and after the addition of MB, in the absence and presence of dsDNA. In this case, a shift of the bands from 1400 cm^{-1} and 1628 cm^{-1} to longer wavelengths was observed, but also the appearance of a new Raman band at approx. 1580 cm^{-1} was observed. It should be noted that the band obtained at 1400 cm^{-1} corresponds to the elongation vibrations of the (C_9-N_{10}), (C_3-N_2) and (C-N) molecular bonds, while the band at 1628 cm^{-1} corresponds to the elongation vibrations of the (C-C)/(C-N) aromatic structure [52]. This demonstrates a vibrational mode shift observed for both the aromatic structure and the ends of the MB molecule chain, and it was correlated with the intercalation of the entire structure within nucleic acids. Also, no band

disappearances were observed, thus concluding that the MB chain structure remained intact after the interaction with nucleic acids.
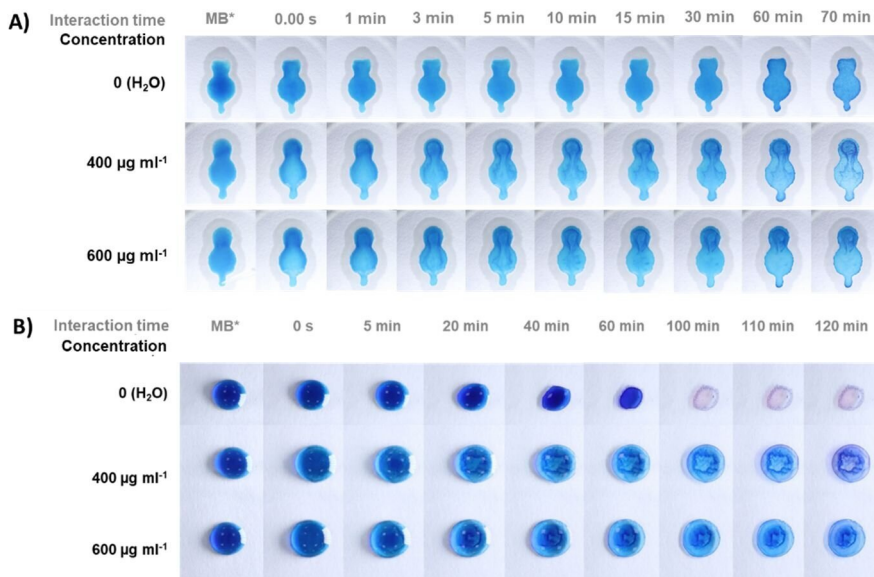
Figure 7.9. Recordings of the interaction between 1 mM MB and dsDNA at different concentrations, **A)** on paper substrate and **B)** on glass slide. MB* represents the visualization of the methylene blue distribution prior to any addition.
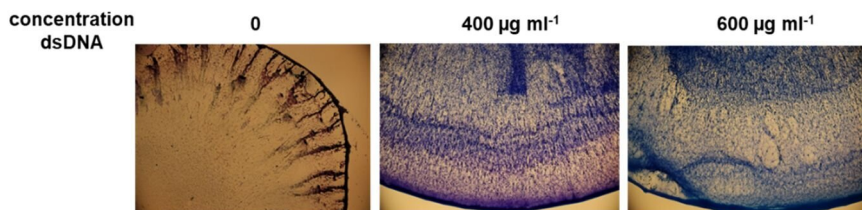
Figure 7.10. Optical microscopy images taken of dried MB droplets on glass slides in the absence and presence of dsDNA.

    Raman spectroscopy measurements were complemented by Vis-NIR spectrophotometry investigations, **Figure 7.11 C)**, observing an increase in the reflectance spectra of MB-saturated chromatographic paper following successive additions of dsDNA, but also a shift of the maximum towards shorter wavelengths. The increase in reflectance implies a decrease in the absorbance of MB molecules. These results demonstrate a decrease in the number of free MB molecules that can interact with the electromagnetic radiation following the addition of nucleic acids, an effect due to their intercalation between the nitrogenous bases of dsDNA.
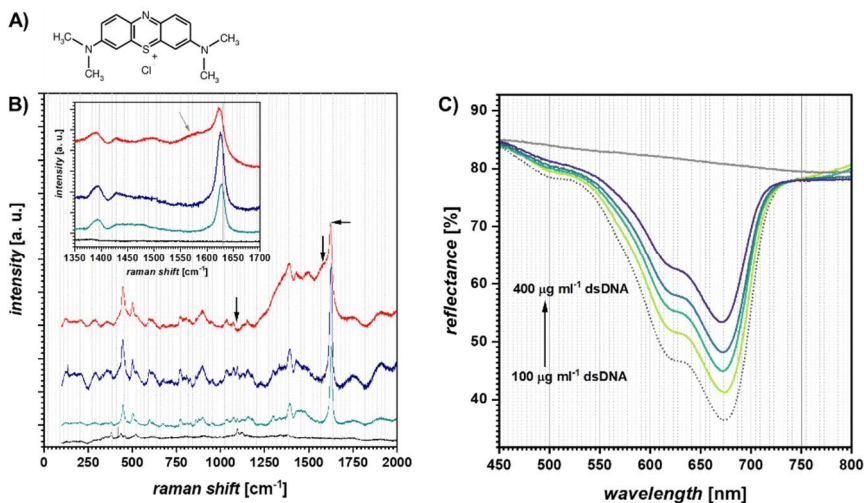
Figure 7.11. A) Chemical structure of MB. **B)** Raman spectra recorded on chromatography paper (black), paper with 10 mM MB (turquoise) and paper with MB in the presence of 100 (blue) and 1000 (red) µg ml^{-1} dsDNA. **C)** Reflectance spectra of chromatographic paper saturated with 100 µM MB before and after successive additions of 100 µg ml-1 dsDNA. Inset: magnified view of displaced bands following interaction between MB and dsDNA.

For the detection, the chromatographic paper sensor reservoir was saturated with 40 µl of 1 mM MB in phosphate buffer pH 6.9. The technique used for detection was differential pulse voltammetry which showed a cathodic current peak due to the MB reduction reaction. Subsequently, successive additions of 4 µl of solutions of different dsDNA concentrations were made and a voltammogram was recorded after each addition, **Figure 7.12**. These experiments showed a progressive decrease in the intensity of the MB reduction-specific current with increasing dsDNA concentration. As previously mentioned, MB interacts with dsDNA by intercalation between its nitrogenous bases, which leads to a decrease in the number of free molecules in solution available to perform a charge transfer with the electrode surface. This interaction between dsDNA and MB was previously revealed by spectroscopic measurements, thus demonstrating that the decrease in current intensity is not due to blockage of the electrode surface by adsorption of MB or nucleic acids, but to the interaction between the two compounds.

The experimental results on the variation of current density as a function of nucleic acid concentration were interpolated with a line described by $\Delta j = a + b \log_2([dsDNA]/ \mu g\ ml^{-1})$, where $a = (24.94 \pm 1.46)$ µA cm^{-2}, and $b = (49.25 \pm 1.63)$ µA cm^{-2} (µg ml^{-1}) $^{-1}$, for which R^2 = 0.996 was obtained, in the linearity range between 0.5 and 32.0 µg ml^{-1}. The limit of detection of (0.147 $\pm$ 0.005) µg ml^{-1}, the sensitivity of (49.25 $\pm$ 1.63) µA cm^{-2}(µg ml^{-1})$^{-1}$ and the limit of quantification of (0.491 $\pm$ 0.016) µg ml^{-1} were obtained.

The applicability of the sensors for the detection and quantification of nucleic acids was also investigated by electrochemical impedance spectroscopy, **Figure 7.13**. In this case, the impedance of the system was measured in phosphate buffer pH 6.9 at open circuit potential with periodic injections of dsDNA.
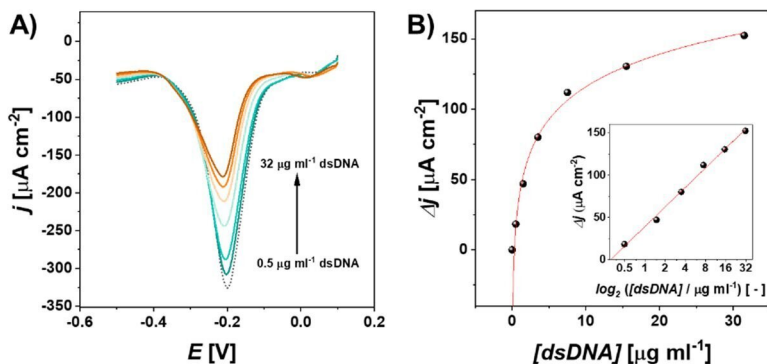
Figure 7.12. A) Voltammograms performed in the presence of MB in phosphate buffer pH 6.9 with additions of different concentrations of dsDNA. **B)** Calibration curve of experimental data. Inset: log-log representation of the experimental points.

Additions of dsDNA led to an increase in the imaginary component of the impedance and thus the total impedance of the system. Since nucleic acids are a dielectric material, the increase in impedance is a direct measure of the increase in the dielectric constant of the paper-dsDNA complex due to the increase in nucleic acid concentration. There were observed a progressive increase in the imaginary component of the system impedance for each addition of dsDNA and the stability of the response over time at each value reached.
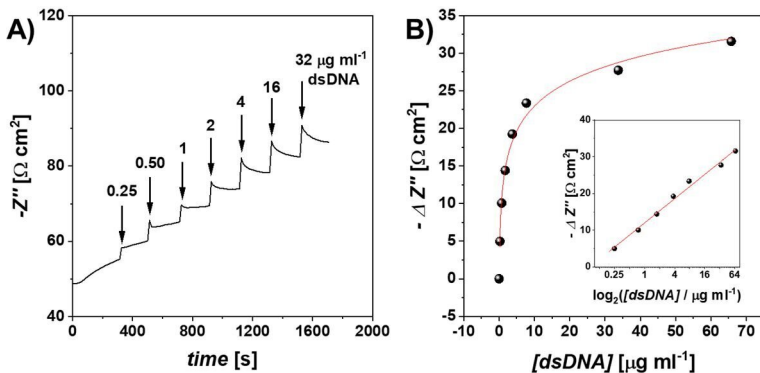
Figure 7.13. Electrochemical impedance spectroscopy performed in open circuit with successive additions of dsDNA. **A)** Variation of the imaginary component and **B)** calibration curve.

The variation of the imaginary impedance component as a function of nucleic acid concentration was interpolated with a line described by the equation $\Delta Z'' = a + b\ log_2([dsDNA]/\mu g\ ml^{-1})$, where $a = (18.72 \pm 0.69)$ Ω, and $b = (17.15 \pm 0.69)$ Ω cm^2 (μg ml^{-1})$^{-1}$, for which R^2 = 0.994 was obtained, in the linearity range from 0.5 to 64.0 μg ml^{-1}. The limit of detection of (0.25 ± 0.01) μg ml^{-1}, the sensitivity of (17.15 ± 0.69) Ω cm^2 (μg ml^{-1})$^{-1}$ and the limit of quantification of (0.85 ± 0.034) μg ml^{-1} were obtained.

Chapter 8. Conclusions and final remarks

The main focus of this thesis was the study of the interaction between fluids and fibrillar porous media, the main attention being focused on the diffusion process. The results obtained were used for the fabrication of portable sensors consisting of paper substrate and metalized polymer fiber electrodes. Thus, the thesis was structured in two parts specific to each field of study.

In the first part of the thesis the theoretical descriptions of the diffusion phenomenon were introduced. The aim was to comprehensively describe the process, considering both the advancement of the fluid into the porous substrate and the evolution of the fluid droplet interface remaining at the substrate surface.

In order to efficiently analyse the phenomenon, a numerical code was developed in MATLAB for automatic processing of the images resulting from recordings of the difussion process. The code was developed to identify the interface of the droplet, and evaluate the time evolution of parameters such as diameter, height, volume and contact angle. The originality of the developed code is its applicability to any type of fluid droplet, without requiring the use of chemical compounds for fluid colouring, which could influence its behaviour. In addition, using this code, the analysis of the diffusion process can be performed without prior knowledge of the material parameters of the fluid, such as viscosity or surface tension, the evolution of the interface over time being sufficient for the numerical evaluation of the parameters of phenomenological interest.

The experimental studies on the diffusion process were focused on the behaviour of simple and complex fluids, both for the case of an "infinite" medium (unbounded radial diffusion), and in the presence of hydrophobic barriers. The influences of the fluid material properties on the diffusion process were analysed, and trends in velocity variation as a function of fluid viscosity, as well as retention of dissolved molecules in the fluid as a function of chemical compound and solution concentration were identified. By image analysis, the concentration distribution of liquid-phase molecules diffusing through the porous medium could be evaluated. Furthermore, with the developed code it was possible to analyse the droplet behaviour at the surface of the substrate and to evaluate the diffusion velocity and flow rate through the paper.

In the second part of the thesis, flexible porous materials consisting of polymer fiber meshes were fabricated by electrospinning and rotary-jet spinning. By investigating the morphology of the resulting meshes, the influence of environmental, process and material parameters on the two manufacturing processes was analysed. At this stage a MATLAB code was developed for the analysis of the surface porosity of the materials, from the images obtained by scanning electron microscopy. The structure of polymer meshes was investigated to evaluate the possibility of fabricating absorbent substrates and flexible electrodes. The conductivity of the meshes was ensured by magnetron sputtering of thin metallic layers, and the electrical and electrochemical properties were investigated experimentally for different densities of the polymer layer formed. Moreover, the fabricated porous substrates were observed to have a morphology suitable for the development of filtering materials, due to the small pore size in the micrometer range.

For the proposed application, a procedure for fabricating a portable electrochemical cell with porous substrate and polymeric mesh electrodes was implemented, being the first example of such an integrated architecture. In a first step, hydrophobic barriers were 3D printed in the porous substrate, and multiple geometries as well as different printing parameters and heat treatment conditions were investigated in order to achieve the full confinement of fluid. Selective metallization of the polymer meshes was achieved by CAD designing and 3D printing of masks with photopolymer resin. To develop a sensor with optimal operating parameters, four

46

configurations with different electrode placement on the paper were fabricated. Their characteristics were studied electrochemically by cyclic voltammetry in the presence of redox samples (potassium hexacyanoferrate and methylene blue). The configuration considered optimal was then characterized voltammetrically in electrolyte media with different pH values and by electrochemical impedance spectroscopy, in order to model the device with an equivalent electrical circuit. Facile handling of the developed sensor was ensured by fabricating 3D printed supports equipped with copper or platinum plates for an ohmic contact with the electrodes.

Finally, two applications were developed for the electrochemical sensor, which were aimed at the detection and quantification of analytes present in sweat, as well as nucleic acids. These compounds were chosen with the aim of developing a portable biosensor, which can reduce the energy requirements involved in classical analysis in a clinical laboratory. The sensor has been designed so that it can be used outside a dedicated laboratory and allows integration with electronic circuits powered by low-voltage batteries. In the first application, the possibility of detecting reaction by-products between an analyte and an enzyme, at different applied potentials, in basic or acidic media was evaluated. Subsequently, the detection and quantification of glucose in both buffer solutions, and artificial sweat was performed. The detection limit obtained for the determination of glucose in artificial sweat was below the normal values in human sweat, thus demonstrating the applicability of the fabricated device. In the second application, the detection and quantification of nucleic acids was performed both in the presence of methylene blue, and in the absence of any electrochemical marker. The interaction between nucleic acids and methylene blue on the paper substrate was investigated by optical and spectroscopic methods (UV-Vis-NIR and Raman), demonstrating that molecular reactions can take place in a porous substrate without being influenced by the structure of the material. All the applications could be performed in the potential range [-0.5; +0.8] V, thus making it feasible to integrate and power the device with low voltage batteries.

Personal contributions

The contributions of this thesis regard the fields of fluid mechanics and electrochemical sensors. In the first case, the study was focused describing the diffusion phenomena of simple and complex fluids in porous media. In the second case, procedures for the fabrication, characterisation and application of sensors fabricated from layers of porous media were implemented. Thus, the main contributions to the fields are:

1. Development of an algorithm and a numerical code in MATLAB for automatic image processing for extracting and analysis parameters related to the diffusion phenomenon.
2. Optimisation of hydrophobic barriers fabrication procedures in porous media.
3. Experimental investigation of the diffusion process and description of flow regimes.
4. Numerical description of the dependence between diffusion velocity and fluid viscosity.
5. Investigation of the concentration-dependent retention process of molecules and development of an imaging analysis procedure for approximating the concentration variation of the molecules on the surface of the porous media.
6. Optimisations of the electrospinning and rotary-jet spinning processes for fabricating porous materials, by studying the influences of material, environment and process parameters on the morphology of the resulting fibers.
7. Development of a numerical code in MATLAB for the evaluation of surface porosity.
8. Evaluation of electrical and electrochemical characteristics of metallized porous structures as a function of their density.

9. Development of the fabrication procedure of an electrochemical cell composed of electrodes represented by metallized fibrillar porous surfaces and hydrophilic porous substrate modified with hydrophobic barriers.
10. Electrochemical characterization of the fabricated device, investigating multiple architectures in two and three electrode configuration.
11. Development of detection procedures for hydrogen peroxide, nicotinamide adenine dinucleotide, glucose and nucleic acids, in the fabricated device.
12. Investigation of molecular reactions in the porous substrate by spectroscopic measurements.

The studies carried out in this thesis revealed the possibility of applying porous media of different structures for the development of a portable device, which can perform an analysis of the chemical compounds present in various fluids. The results obtained led to a patent for an electrochemical cell with an integrated flexible fibrillar structure.

Future perspectives

Fluid diffusion in fibrillar porous media is a complex process due to the inhomogeneities of the structure and chemical interactions between fluid and fibre surface. The studies presented in the current thesis present the basis for understanding the phenomenology, and following these experiments on the chemical modification of paper and analysis of the influence of this process on the transport of complex fluids are envisioned. In this way, selective transport pathways can be obtained, or selective separation of chemical compounds from complex fluids can be achieved.

To extend the applicability of porous media, their ability to capture and retain molecules or nano-/micro-particles dissolved in liquid media will be evaluated, in order to fabricate filtering materials. Studies will also be carried out on the ability of porous media to capture vapours from the ambient atmosphere to extend the applicability of the sensor in the detection of aerosolised chemical compounds.

As the morphology of the porous medium influences the interaction with fluids, the process of fabricating polymer meshes will be evaluated with different types of synthetic (such as nylon) or natural polymers (polycaprolactone, polylactic acid), which due to their material properties can confer unique characteristics to the formed layers (flexibility, mechanical strength, biodegradability). The rheological properties of different polymer solutions, the influence of environmental and process parameters, and the optical and mechanical properties of the resulting meshes will be investigated.

The applications presented in this thesis are in the biomedical field, but the applicability of the sensor can be extended by using markers, enzymes or metallic or semiconducting materials adapted to the selective interaction with other ions or molecules of interest. Thus, it is envisaged to perform functionalisation for the detection of contaminants such as toxic chemical compounds or heavy metal ions.

In order to broaden the sensor's applicability, the developed architecture will be integrated with auxiliary elements. In order to offer the functionality outside a scientific laboratory, the device will be integrated with electronic circuits that will fulfil the roles of measurement (thus forming a portable potentiostat) and data transmission to mobile devices. Such an architecture allows measurements to be made using electrical supply from low-voltage batteries. By using additional polymeric substrates, absorption and evaporation processes can be stimulated to develop a wearable biosensor with a constant flow regime.

References (selection)

[1] J. Kim, J. Park, J. Lee, W.G. Lim, C. Jo, J. Lee, Biomass-Derived P, N Self-Doped Hard Carbon as Bifunctional Oxygen Electrocatalyst and Anode Material for Seawater Batteries, Adv. Funct. Mater. 31 (2021) 2010882.

[2] X. Miao, D. Sun, X. Zhou, Z. Lei, Designed formation of nitrogen and sulfur dual-doped hierarchically porous carbon for long-life lithium and sodium ion batteries, Chem. Eng. J. 364 (2019) 208–216.

[3] Y.H. Lee, J.S. Kim, J. Noh, I. Lee, H.J. Kim, S. Choi, J. Seo, S. Jeon, T.S. Kim, J.Y. Lee, J.W. Choi, Wearable textile battery rechargeable by solar energy, Nano Lett. 13 (2013) 5753–5761.

[4] Q. Lai, J. Zheng, Z. Tang, D. Bi, J. Zhao, Y. Liang, Optimal Configuration of N-Doped Carbon Defects in 2D Turbostratic Carbon Nanomesh for Advanced Oxygen Reduction Electrocatalysis, Angew. Chemie. 132 (2020) 12097–12104.

[5] K.R.A. Saravanan, N. Prabu, M. Sasidharan, G. Maduraiveeran, Nitrogen-self doped activated carbon nanosheets derived from peanut shells for enhanced hydrogen evolution reaction, Appl. Surf. Sci. 489 (2019) 725–733.

[6] S.A. Nicolae, P.Á. Szilágyi, M.M. Titirici, Soft templating production of porous carbon adsorbents for CO2 and H2S capture, Carbon N. Y. 169 (2020) 193–204.

[7] Y. Song, J. Phipps, C. Zhu, S. Ma, Porous Materials for Water Purification, Angew. Chemie Int. Ed. 62 (2023) e202216724.

[8] Q. Sun, B. Aguila, J.A. Perman, T. Butts, F.S. Xiao, S. Ma, Integrating Superwettability within Covalent Organic Frameworks for Functional Coating, Chem. 4 (2018) 1726–1739.

[9] X. Luo, X. Yao, Y. Zhang, X. Zheng, G. Xie, Y. Cui, Amperometric biosensing system directly powered by button cell battery for lactate, PLoS One. 14 (2019) e0212943.

[10] R.A. O'Kelly, J.J. Brady, E. Byrne, K. Hooley, C. Mulligan, K. Mulready, P. O'Gorman, P. O'Shea, G. Boran, A survey of point of care testing in Irish hospitals: room for improvement, Ir. J. Med. Sci. 180 (2011) 237–240.

[11] A.C. Sun, D.A. Hall, Point-of-Care Smartphone-based Electrochemical Biosensing, Electroanalysis. 31 (2019) 2–16.

[12] B. Liang, Q. Cao, X. Mao, W. Pan, T. Tu, L. Fang, X. Ye, An Integrated Paper-Based Microfluidic Device for Real-Time Sweat Potassium Monitoring, IEEE Sens. J. 21 (2021) 9642–9648.

[13] F. Criscuolo, I. Ny Hanitra, S. Aiassa, I. Taurino, N. Oliva, S. Carrara, G. De Micheli, Wearable multifunctional sweat-sensing system for efficient healthcare monitoring, Sensors Actuators B Chem. 328 (2021) 129017.

[14] H.R. Lim, Y. Lee, K.A. Jones, Y.T. Kwon, S. Kwon, M. Mahmood, S.M. Lee, W.H. Yeo, All-in-one, wireless, fully flexible sodium sensor system with integrated Au/CNT/Au nanocomposites, Sensors Actuators B Chem. 331 (2021) 129416.

[15] R. Silva, K. Zhao, R. Ding, W.P. Chan, M. Yang, J.S.Q. Yip, G. Lisak, Ion-selective membrane modified microfluidic paper-based solution sampling substrates for potentiometric heavy metal detection, Analyst. 147 (2022) 4500–4509.

[16] T. Saha, T. Songkakul, C.T. Knisely, M.A. Yokus, M.A. Daniele, M.D. Dickey, A. Bozkurt, O.D. Velev, Wireless Wearable Electrochemical Sensing Platform with Zero-Power Osmotic Sweat Extraction for Continuous Lactate Monitoring, ACS Sensors. 7 (2022) 2037–2048.

[17] R. Wang, Q. Zhai, T. An, S. Gong, W. Cheng, Stretchable gold fiber-based wearable textile electrochemical biosensor for lactate monitoring in sweat, Talanta. 222 (2021) 121484.

[18] M. Li, L. Wang, R. Liu, J. Li, Q. Zhang, G. Shi, Y. Li, C. Hou, H. Wang, A highly integrated sensing paper for wearable electrochemical sweat analysis, Biosens. Bioelectron. 174 (2021) 112828.

[19] D.S. Rocha, L.C. Duarte, H.A. Silva-Neto, C.L.S. Chagas, M.H.P. Santana, N.R. Antoniosi Filho, W.K.T. Coltro, Sandpaper-based electrochemical devices assembled on a reusable 3D-printed holder to detect date rape drug in beverages, Talanta. 232 (2021) 122408.

[20] C. Zhou, K. Cui, Y. Liu, S. Hao, L. Zhang, S. Ge, J. Yu, Ultrasensitive Microfluidic Paper-Based Electrochemical/Visual Analytical Device via Signal Amplification of Pd@Hollow Zn/Co Core-Shell ZIF67/ZIF8 Nanoparticles for Prostate-Specific Antigen Detection, Anal. Chem. 93 (2021) 5459–5467.

[21] S. Boonkaew, A. Yakoh, N. Chuaypen, P. Tangkijvanich, S. Rengpipat, W. Siangproh, O. Chailapakul, An automated fast-flow/delayed paper-based platform for the simultaneous electrochemical detection of hepatitis B virus and hepatitis C virus core antigen, Biosens. Bioelectron. 193 (2021) 113543.

[22] D. Lee, J. Bhardwaj, J. Jang, Paper-based electrochemical immunosensor for label-free detection of multiple avian influenza virus antigens using flexible screen-printed carbon nanotube-polydimethylsiloxane electrodes, Sci. Reports 2022 121. 12 (2022) 1–11.

[23] F.G. Ortega, M.D. Regiart, A. Rodríguez-Martínez, D. De Miguel-Pérez, M.J. Serrano, J.A. Lorente, G. Tortella, O. Rubilar, K. Sapag, M. Bertotti, M.A. Fernández-Baldo, Sandwich-Type Electrochemical Paper-Based Immunosensor for Claudin 7 and CD81 Dual Determination on Extracellular Vesicles from Breast Cancer Patients, Anal. Chem. 93 (2021) 1143–1153.

[24] C. Srisomwat, A. Yakoh, N. Chuaypen, P. Tangkijvanich, T. Vilaivan, O. Chailapakul, Amplification-free DNA Sensor for the One-Step Detection of the Hepatitis B Virus Using an Automated Paper-Based Lateral Flow Electrochemical Device, Anal. Chem. 93 (2021) 2879–2887.

[25] S. Khaliliazar, A. Toldrà, G. Chondrogiannis, M.M. Hamedi, Electroanalytical Paper-Based Nucleic Acid Amplification Biosensors with Integrated Thread Electrodes, Anal. Chem. 93 (2021) 14187–14195.

[26] A. Lomae, P. Preechakasedkit, O. Hanpanich, T. Ozer, C.S. Henry, A. Maruyama, E. Pasomsub, A. Phuphuakrat, S. Rengpipat, T. Vilaivan, O. Chailapakul, N. Ruecha, N. Ngamrojanavanich, Label free electrochemical DNA biosensor for COVID-19 diagnosis, Talanta. 253 (2023) 123992.

[27] N. Colozza, S. Tazzioli, A. Sassolini, L. Agosta, M.G. di Monte, K. Hermansson, F. Arduini, Vertical-Flow Paper Sensor for On-Site and Prompt Evaluation of Chloride Contamination in Concrete Structures, Anal. Chem. 93 (2021) 14369–14374.

[28] T. Pholsiri, A. Lomae, K. Pungjunun, S. Vimolmangkang, W. Siangproh, O. Chailapakul, A chromatographic paper-based electrochemical device to determine Δ^9-tetrahydrocannabinol and cannabidiol in cannabis oil, Sensors Actuators B Chem. 355 (2022) 131353.

[29] T.S. Martins, S.A.S. Machado, O.N. Oliveira, J.L. Bott-Neto, Optimized paper-based electrochemical sensors treated in acidic media to detect carbendazim on the skin of apple and cabbage, Food Chem. 410 (2023) 135429.

[30] A. Cioffi, M. Mancini, V. Gioia, S. Cinti, Office Paper-Based Electrochemical Strips for Organophosphorus Pesticide Monitoring in Agricultural Soil, Environ. Sci. Technol. 55 (2021) 8859–8865.

[31] V. Caratelli, G. Fegatelli, D. Moscone, F. Arduini, A paper-based electrochemical device for the detection of pesticides in aerosol phase inspired by nature: A flower-like origami

biosensor for precision agriculture, Biosens. Bioelectron. 205 (2022) 114119.

[32] L. Fiore, V. Mazzaracchio, A. Serani, G. Fabiani, L. Fabiani, G. Volpe, D. Moscone, G.M. Bianco, C. Occhiuzzi, G. Marrocco, F. Arduini, Microfluidic paper-based wearable electrochemical biosensor for reliable cortisol detection in sweat, Sensors Actuators B Chem. 379 (2023) 133258.

[33] E. Kissa, Wetting and Wicking. 66 (1996) 660–668.

[34] D.A. Nield, A. Bejan, Convection in porous media, Convect. Porous Media. (2013) 1–778.

[35] L. Durlofsky, J.F. Brady, Analysis of the Brinkman equation as a model for flow in porous media, Phys. Fluids. 30 (1987) 3329–3341.

[36] J. Bear, Dynamics of Fluids in Porous Media, Dover Publications, New York, 1972.

[37] S. Srinivasan, K.R. Rajagopal, On the flow of fluids through inhomogeneous porous media due to high pressure gradients, Int. J. Non. Linear. Mech. 78 (2016) 112–120.

[38] S. Whitaker, Flow in porous media I: A theoretical derivation of Darcy's law, Transp. Porous Media. 1 (1986) 3–25.

[39] P.-G. de Gennes, F. Brochard-Wyart, D. Quéré, Capillarity and Wetting Phenomena - Drops, Bubbles, Pearls, Waves, Springer New York, 2004.

[40] S.H. Davis, L.M. Hocking, Spreading and imbibition of viscous liquid on a porous base, Phys. Fluids. 11 (1999) 48–57.

[41] T. Gillespie, The spreading of low vapor pressure liquids in paper, J. Colloid Sci. 13 (1958) 32–50.

[42] A. Borhan, K.K. Rungta, On the radial spreading of liquids in thin porous substrates, J. Colloid Interface Sci. 154 (1992) 295–297.

[43] A. Borhan, K.K. Rungta, An experimental study of the radial penetration of liquids in thin porous substrates, J. Colloid Interface Sci. 158 (1993) 403–411.

[44] D. Botta, I. Magos, C. Balan, Influence of Viscosity on Radial Diffusion of Fluids in Paper Substrates, 12th Int. Symp. Adv. Top. Electr. Eng. ATEE 2021. (2021).

[45] D. Soulis, V. Pagkali, C. Kokkinos, A. Economou, Plot-on-demand integrated paper-based sensors for drop-volume voltammetric monitoring of Pb(II) and Cd(II) using a bismuth nanoparticle-modified electrode, Microchim. Acta. 189 (2022) 1–10..

[46] A. Cioffi, M. Mancini, V. Gioia, S. Cinti, Office Paper-Based Electrochemical Strips for Organophosphorus Pesticide Monitoring in Agricultural Soil, Environ. Sci. Technol. 55 (2021) 8859–8865.

[47] Y. Xiao, N. Wu, L. Wang, L. Chen, A Novel Paper-Based Electrochemical Biosensor Based on N,O-Rich Covalent Organic Frameworks for Carbaryl Detection, Biosensors. 12 (2022) 899.

[48] H. Li, W. Wang, Q. Lv, G. Xi, H. Bai, Q. Zhang, Disposable paper-based electrochemical sensor based on stacked gold nanoparticles supported carbon nanotubes for the determination of bisphenol A, Electrochem. Commun. 68 (2016) 104–107.

[49] D. Botta, I. Enculescu, C. Balan, V.C. Diculescu, Integrated architectures of electrodes and flexible porous substrates for point-of-care testing, Curr. Opin. Electrochem. 42 (2023) 101418.

[50] A.J. Bandodkar, J. Wang, Non-invasive wearable electrochemical sensors: a review, Trends Biotechnol. 32 (2014) 363–371.

[51] L.B. Baker, Physiology of sweat gland function: The roles of sweating and sweat composition in human health, Temperature. 6 (2019) 211–259.

[52] S. Dutta Roy, M. Ghosh, J. Chowdhury, Adsorptive parameters and influence of hot geometries on the SER(R) S spectra of methylene blue molecules adsorbed on gold nanocolloidal particles, J. Raman Spectrosc. 46 (2015) 451–461.